3

Solid State Research

1968

Prepared under Electronic Systems Division Contract AF 19(628)-5167 by

Lincoln Laboratory

MASSACHUSETTS INSTITUTE OF TECHNOLOGY

Lexington, Massachusetts

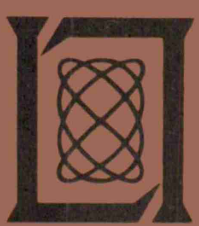

The work reported in this document was performed at Lincoln Laboratory, a center for research operated by Massachusetts Institute of Technology, with the support of the U.S. Air Force under Contract AF 19(628)-5167.

3

Solid State Research

1968

Issued 14 October 1968

Lincoln Laboratory

MASSACHUSETTS INSTITUTE OF TECHNOLOGY

Lexington, Massachusetts

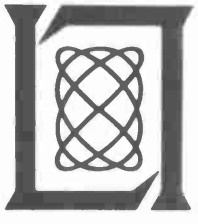

ABSTRACT

This report covers in detail the solid state research work at Lincoln Laboratory for the period 1 May through 31 July 1968. The topics covered are Solid State Device Research, Optical Techniques and Devices, Materials Research, and Physics of Solids.

Accepted for the Air Force
Franklin C. Hudson
Chief, Lincoln Laboratory Office

INTRODUCTION

I. SOLID STATE DEVICE RESEARCH

Infrared radiation in the wavelength region between 300 and 1000 μ has been modulated utilizing free carrier absorption by impact ionized electrons in germanium. Modulation depths of up to 20 percent at 902 μ and several percent at 337 μ have been observed with time constants less than 0.1 μsec.

Guard rings consisting of epitaxial n-GaAs have been grown for GaAs p-n junction and Schottky barrier avalanche diodes utilizing the $AsCl_3$-Ga-H_2 flow system. The breakdown voltage for the guarded structures is higher than for those without a guard ring, and in avalanche breakdown light is emitted nearly uniformly across the diode, whereas in unguarded diodes light emission is at the perimeter. The guarded diodes have been used as avalanche photodetectors and show a gain in excess of 100 when biased near reverse breakdown.

The combined effects of applied DC bias and short wavelength radiation on the properties of InSb-MOS infrared detectors have been further investigated. Several processes have been isolated and identified. For photon energies greater than 0.5 to 2.0 eV, depending upon the initial charge state of the system, electrons are photoemitted from the InSb into the oxide where they may become trapped. For photon energies greater than 1.0 to 3.0 eV, again depending upon the initial charge state of the system, the oxide layer becomes photoconductive. These effects are reflected in the response of the InSb-MOS detector to 3.9-μ InAs diode radiation and appear to be a controlling factor in the performance of the device.

High-resistivity surface layers up to 4 μ deep have been produced in 4-ohm-cm p-type ZnTe by bombardment with approximately 10^{14} protons/cm^2 from a 400 kV Van de Graaff generator. Contact to contact resistance between ohmic contacts on the front surface increased from about 200 to greater than 10^9 ohms after bombardment.

A study of metal inclusions and low-angle grain boundaries in $Pb_{1-x}Sn_xTe$ crystals has indicated that these defects are due to constitutional supercooling during growth. This explanation indicates that these defects may be avoided by growing from a sufficiently tellurium-rich melt, by growing in a steep temperature gradient or by decreasing the growth rate. Crystals grown from a $(Pb_{1-x}Sn_x)_{0.49}Te_{0.51}$ melt have been found to be essentially free of these macroscopic defects.

The properties of bismuth doped $Pb_{1-x}Sn_xTe$ diode lasers have been examined for x in the range $0.24 \lesssim x \lesssim 0.27$, where it is difficult to obtain high carrier concentration n-type material by deviations from stoichiometry only. The main effect of doping with Bi is believed to be a shift in the composition at which n = p to the Te-rich side of the stoichiometric line. This allows larger n-type carrier concentrations to be obtained with shorter annealing times. The Bi doping also reduces the laser threshold current densities at both 12° and 77°K. In fact, at 77°K undoped diodes in this composition range did not exhibit laser emission up to 30,000 A/cm^2 while doped diodes had threshold currents between 1000 and 5000 A/cm^2.

II. OPTICAL TECHNIQUES AND DEVICES

A 9-meter CO_2 amplifier with an average bore of 25 mm has yielded a small signal gain of 4.8 db/meter. This gain was for a sealed off gas mixture and compares favorably with the measured gain of a flowing gas amplifier.

The usefulness of the f-number criterion for the achievement of optimum "optical" heterodyning has been demonstrated experimentally.

Some preliminary propagation measurements and calculations at 10 μm are being made in anticipation of the requirements and capabilities of the Millstone Hill CO_2 laser radar.

Variation of the refractive index with temperature enables continuous tuning of the $Pb_{1-x}Sn_xTe$ diode laser. Beat frequencies from essentially zero to 3.5 GHz have been observed in heterodyne experiments using the P_{18}, P_{20}, and P_{22} lines from a CO_2 laser. Preliminary observations were made of the Lorentzian-shaped laser line profile. Also measured was the frequency response of a Ge:Cu detector similar to one scheduled for use in the CO_2 Doppler radar system.

III. MATERIALS RESEARCH

A number of garnets containing tellurium, with the type formula $\{A_3\}[Te_2](B_3)O_{12}$, have been prepared by sintering stoichiometric mixtures of oxides and carbonates. They include the first garnets in which Co^{+2} ions occupy only tetrahedral sites and a series of rare-earth garnets in which B is Li^+ and A is triply charged Pr, Nd, Sm, Eu, Gd, Tb, Dy, Ho, Er, Tm, Yb, or Lu.

The atmospheric pressure phase of $CdCr_2Se_4$, which has the cubic spinel structure, is transformed at high pressures and elevated temperatures into a phase with the monoclinic defect-NiAs structure. In contrast with the spinel phase, which is a ferromagnetic semiconductor, the high-pressure phase is metallic and nonmagnetic.

A high-pressure form of $CsNiF_3$ has been prepared by reaction of CsF and NiF_2 at 65 kbars and 700°C. This phase has a hexagonal structure isomorphous with that of the atmospheric pressure phase of $RbNiF_3$ and, like that phase, is a light yellow, transparent ferrimagnet.

The atmospheric pressure phase of $SrIrO_3$ has been found to have a monoclinic structure closely related to that of the atmospheric pressure phase of $RbNiF_3$. At high pressures and elevated temperatures, $SrIrO_3$ is transformed into a phase with orthorhombically distorted perovskite structure.

An extensive summary of the crystallographic and magnetic properties of perovskite and perovskite-related compounds, with an interpretive introduction and over 1500 references, has been prepared for the Landolt-Bornstein Tabellen.

The low-lying energy levels of U^{3+} compensated by Na^{+1} in CaF_2:$NaUF_4$ have been determined by infrared absorption measurements. Because of the high proportion (90%) of orthorhombic site symmetry and the relatively high energy (607 cm^{-1}) of the terminal level for

laser emission, the threshold for pulsed laser action in this material is less than 1 joule at 77°K.

A method has been developed for the analysis of Zn-Te-Se alloys which is accurate to within a few parts per thousand for each component. The Se and Te are determined by classical oxidation-reduction methods using automatic titration equipment, and Zn is determined by an x-ray fluorescence method.

IV. PHYSICS OF SOLIDS

Recent optical and transport data for NiO indicate that the localized crystal-field spectrum and the band-like, nonactivated mobility are incompatible properties if only d-electrons are considered; electron band states are also necessary. A procedure is suggested for portraying both these properties on a single diagram, analogously to the band structure diagram of simpler materials.

The study of oscillatory magnetoreflection in bismuth-antimony alloys at low temperatures indicates an increase of energy gap and effective mass with increasing antimony concentration in the range of composition $0 \lesssim \%\ \mathrm{Sb} \lesssim 15$. In contrast to the semimetallic nature of bismuth, the higher antimony alloys exhibit the semiconducting behavior suggested by transport measurements.

Using a generalization of a method developed by P. Resibois for a pure interacting Fermi gas, the transport properties for weak and slowly varying disturbances have been investigated. Coefficients of the transport equation have been calculated for (a) a neutral or charged Fermi liquid in the presence of random impurities (b) dynamically independent fermions in the presence of dilute but arbitrarily strong impurity scattering centers and (c) a Fermi liquid in the generalized random phase approximation in the presence of dilute, but arbitrarily strong impurity scattering centers.

Measurements of the magnetic properties of MnAs under pressure have been extended to include paramagnetic susceptibility in the high temperature $B8_1$ phase. It was found that, unless third-order strain effects are included, even a generalized form of the Bean-Rodbell thermodynamic theory is unable to explain the change in sign at the hexagonal-orthorhombic transition of the pressure dependence of the paramagnetic Curie temperature. The fact that this sign change is restricted to a narrow temperature interval is attributed to large changes in the exchange parameters through the narrow transition region where the manganese atomic moment is changing from a high- to a low-spin value.

The high-temperature expansion method, applied to the Heisenberg model, has been used to investigate the dependence of the zero-field susceptibility exponent on spin quantum number in ferromagnets and to compare the exponent of the staggered susceptibility of two- and three-dimensional antiferromagnets with other recent work. An exact solution for a linear chain of isotropically interacting classical spins of arbitrary dimensionality has been obtained.

Preliminary experiments of light scattering from ferromagnetic $CrBr_3$ and ferromagnetic $RbNiF_3$ have been carried out with an argon ion laser. Both elastic (Rayleigh) scattering

near the transition temperature and inelastic (Raman) scattering over a wider temperature range are being investigated.

An attempt has been made to measure by high resolution Raman scattering at liquid helium temperatures the splitting, $\Delta\omega = \omega_L - \omega_T$, of the 128 cm^{-1} Raman vibration in quartz. Even at 5°K, the linewidth ($\delta\omega = 0.05 \pm 0.01$ cm^{-1}) is about twice the gap ($\Delta\omega = 0.02 \pm 0.01$ cm^{-1}); thus, the doublet was not resolved.

CONTENTS

	Abstract	iii
	Introduction	iv
	Organization	ix
	Reports by Authors Engaged in Solid State Research	x
I.	SOLID STATE DEVICE RESEARCH	1
	A. Modulation of Far-Infrared Radiation by Impact Ionized Free Carriers in Germanium	1
	B. Epitaxially Grown Guard Rings for GaAs Diodes	3
	C. Characteristics of InSb-MOS Detectors	7
	D. High Resistivity Layers Produced in ZnTe by Proton Bombardment	10
	E. Metal Inclusions and Cellular Substructure in $Pb_{1-x}Sn_xTe$ Single Crystals	10
	F. Bismuth Doped $Pb_{1-x}Sn_xTe$ Diode Lasers	13
II.	OPTICAL TECHNIQUES AND DEVICES	17
	A. 100-Watt CO_2 Amplifier	17
	B. Optical Aspects of Optimum Laser Heterodyning	18
	C. Atmospheric Propagation Effects at 10 μm	18
	D. Tunable Infrared Laser Heterodyne Experiments	19
III.	MATERIALS RESEARCH	27
	A. Preparation of Tellurate Garnets $\{A_3\}[Te_2](B_3)O_{12}$	27
	B. Polymorphism in $CdCr_2Se_4$ at High Pressure	28
	C. High Pressure Form of $CsNiF_3$ – A Transparent Ferrimagnet	31
	D. Low and High Pressure Forms of $SrIrO_3$	33
	E. Crystallographic and Magnetic Properties of Perovskite and Perovskite-Related Compounds	33
	F. Low-Lying Energy Levels and Laser Action of U^{+3} in CaF_2:$NaUF_4$	35
	G. Chemical Analysis of Zn-Te-Se Alloys	37
IV.	PHYSICS OF SOLIDS	39
	A. Electronic Band Structure	39
	B. Transport Phenomena	41
	C. Magnetism	42
	D. Scattering Experiments with Lasers	46

ORGANIZATION

SOLID STATE DIVISION

A. L. McWhorter, *Head*
P. E. Tannenwald, *Associate Head*
M. J. Hudson, *Assistant*
E. P. Warekois

SOLID STATE THEORY

H. J. Zeiger, *Leader*
M. M. Litvak, *Assistant Leader*

Argyres, P. N.
Brine, N. S.
Chinn, S. R.*
Dresselhaus, G. F.
Hamilton, D. C.
Hanus, J.
Kaplan, T. A.
Kelly, P. L.
Kleiner, W. H.
Landon, S. N.
Larsen, D. M.
Malinowski, M. E.†
Palm, B. J.‡
Sigel, J. L.
Stanley, H. E.

OPTICS AND INFRARED

R. H. Kingston, *Leader*
R. J. Keyes, *Assistant Leader*

Bates, D. H.
Bostick, H. A.
Carbone, R. J.
Freed, C.
Gilmartin, T. J.
Hinkley, E. D.
Longaker, P. R.
McPhie, J. M.
O'Donnell, R. G.
Quist, T. M.
Ross, A. H. M.
Sullivan, F. M.
Swezey, L.
Zimmerman, M. D.

ELECTRONIC MATERIALS

J. B. Goodenough, *Leader*
A. J. Strauss, *Associate Leader*

Anderson, C. H., Jr.
Andrews, H. I.*
Apelian, D.†
Arnott, R. J.
Banus, M. D.
Batson, D. A.
Brebrick, R. F., Jr.
Button, M. J.
Capes, R. N.
Delaney, E. J.
England, R. E.
Fahey, R. E.
Ferretti, A.
Finn, M. C.
Iseler, G. W.
Kafalas, J. A.
Kasper, H. M.
LaFleur, W. J.
Lavine, M. C.‡
Longo, J. M.
Mastromattei, E. L.
O'Connor, J. R.
Owens, E. B.
Plonko, M. C.
Raccah, P. M.
Reed, T. B.
Roddy, J. T.
Searles, I. H.
Smith, F. T. J.
Steininger, J. A.
Wheatley, G. E.

SOLID STATE PHYSICS

J. G. Mavroides, *Leader*
G. B. Wright, *Assistant Leader*

Blum, F. A.
Brandt, R. C.
Burke, J. W.
Carman, R. L.*
Crooker, P. P.
Dresselhaus, M. S.‡
Dwight, K., Jr.
Feinleib, J.
Feldman, B.
Fulton, M. J.
Groves, S. H.
Henrich, V. E.
Johnson, E. J.
Kernan, W. C.
Kolesar, D. F.
Krag, W. E.
Melngailis, J.
Menyuk, N.
Murphy, H. C.
Nicoli, D.†
Nill, K. W.
Parker, C. D.
Perry, F. H.
Pine, A. S.
Scouler, W. J.
Stickler, J. J.*
Strahm, N. D.*
Tichovolsky, E. J.*
Waldman, J.*
Weber, R.

APPLIED PHYSICS

J. O. Dimmock, *Leader*
T. C. Harman, *Assistant Leader*
I. Melngailis, *Assistant Leader*

Brueck, S.*
Butler, J. F.
Calawa, A. R.
Carter, F. B.
Caswell, F. H.
Clough, T. F.
Donaldson, P. L.
Donnelly, J. P.
Ferrante, G.
Foyt, A. G.
Hurwitz, C. E.
Lindley, W. T.
Mooradian, A.
Murphy, R. A.*
Oliver, M. R.*
Paladino, A. E.
Phelan, R. J., Jr.
Stillman, G. E.
Ward, J. H. R., III
Wolfe, C. M.
Youtz, P.

---

* Research Assistant
† Summer Staff
‡ Part Time

REPORTS BY AUTHORS ENGAGED IN SOLID STATE RESEARCH

15 May through 15 August 1968

PUBLISHED REPORTS

Journal Articles*

JA No.			
3134A	Epitaxial Gallium Arsenide for High-Efficiency Gunn Oscillators	C.M. Wolfe A.G. Foyt W.T. Lindley	Electrochem. Technol. 6, 208 (1968)
3149	Magnon-Phonon Coupling in Metallic Films	R. Weber	Phys. Rev. 169, 451 (1968)
3162	Design and Short-Term Stability of Single-Frequency CO_2 Lasers	C. Freed	IEEE J. Quant. Electron. QE-4, 404 (1968)
3169	Intense Mercury-Vapor Green-Band Emission	R.J. Carbone M.M. Litvak	J. Appl. Phys. 39, 2413 (1968)
3186	Light Scattering from Single-Particle Electron Excitations in Semiconductors	A. Mooradian	Phys. Rev. Letters 20, 1102 (1968), DDC 671287
3192	Spin-Orbit-Coupling Effects in Transition-Metal Compounds	J.B. Goodenough	Phys. Rev. 171, 466 (1968)
3218	Band Model for Transition-Metal Chalcogenides Having Layer Structures with Occupied Trigonal-Bipyramidal Sites	J.B. Goodenough	Materials Res. Bull. 3, 409 (1968), DDC 671274
3220	Type Conversion and p-n Junctions in n-CdTe Produced by Ion Implantation	J.P. Donnelly A.G. Foyt E.D. Hinkley W.T. Lindley J.O. Dimmock	Appl. Phys. Letters 12, 303 (1968)
3240	Long-Wavelength Infrared $Pb_{1-x}Sn_x$ Te Diode Lasers	J.F. Butler T.C. Harman	Appl. Phys. Letters 12, 347 (1968)
3249	Effect of Pressure on the Structure and Magnetic Properties of $RbNiF_3$	J.A. Kafalas J.M. Longo	Materials Res. Bull. 3, 501 (1968)

* Reprints available.

JA No.			
3256	Location of Electron and Hole Carriers in Graphite from Laser Magnetoreflection Data	P.R. Schroeder* M.S. Dresselhaus A. Javan*	Phys. Rev. Letters 20, 1292 (1968)
3260	Band Antiferromagnetism and the New Perovskite $CaCrO_3$	J.B. Goodenough J.M. Longo J.A. Kafalas	Materials Res. Bull. 3, 471 (1968)
3266	Growth of CdSe Single Crystals by Temperature Gradient Solution Zoning in Excess Se	J.M. Steininger	Materials Res. Bull. 3, 595 (1968)
3270	Microwave Acoustic Amplification in n-InSb at 9 GHz	K.W. Nill	Phys. Rev. Letters 21, 82 (1968)

* * * * *

UNPUBLISHED REPORTS

Journal Articles

JA No.			
3210	Si-Te System: Partial Pressures of Te_2 and SiTe and Thermodynamic Properties from Optical Density of the Vapor Phase	R.F. Brebrick	Accepted by J. Chem. Phys.
3255	Intermediate Coupling Polaron Effective Mass	D.M. Larsen	Accepted by Phys. Rev.
3273	Optical Heterodyne Detection at 10.6 μm of the Beat Frequency Between a Tunable $Pb_{0.88}Sn_{0.12}Te$ Diode Laser and a CO_2 Gas Laser	E.D. Hinkley T.C. Harman C. Freed	Accepted by Appl. Phys. Letters
3274	Magnetic Resonance	R. Weber	Accepted by Magnetism and Magnetic Materials 1968 Digest (Academic Press, New York)
3275	Descriptions of Outer d Electrons in Thiospinels	J.B. Goodenough	Accepted by J. Phys. Chem. Solids
3276	Far Infrared Photoconductivity in High Purity Epitaxial GaAs	G.E. Stillman C.M. Wolfe I. Melngailis C.D. Parker P.E. Tannenwald J.O. Dimmock	Accepted by Appl. Phys. Letters
3280	Pressure-Induced Structural Changes in the System $Ba_{1-x}Sr_xRuO_3$	J.M. Longo J.A. Kafalas	Accepted by Materials Res. Bull.

* Author not at Lincoln Laboratory.

Reports

JA No.			
3284	Non-Metals	N. Menyuk	Accepted by Magnetism and Magnetic Materials 1968 Digest (Academic Press, New York)
3296	Photoconductivity in Single-Crystal $Pb_{1-x}Sn_xTe$	I. Melngailis T.C. Harman	Accepted by Appl. Phys. Letters
3303	Quenchable Effects of High Pressures and Temperatures on the Cubic Monoxide of Titanium	M.D. Banus	Accepted by Materials Res. Bull.
3316	Preparation of $\{A_3^{2+}\}[Te_2](B_3^{2+})O_{12}$- Garnets	H.M. Kasper	Accepted by Materials Res. Bull.

Meeting Speeches*

MS No.			
1719G, 1719H	Interstellar OH Maser Emission	M.M. Litvak	Seminar, M.I.T., 24 June 1968; Seminar, M.I.T., 14 June 1968
1793B	Polaron Self-Energy Effects in InSb	E.J. Johnson	Seminar, Brown University, 17 July 1968
1882E	Raman Scattering from Elementary Excitations in Solids Using Lasers	A. Mooradian	Seminar, Brown University, 26 June 1968
1954B	Localized vs Collective Descriptions of Magnetic Electrons	J.B. Goodenough	Seminar, Westinghouse Research Laboratory, Pittsburgh, Pennsylvania, 16 May 1968
2141C	Magneto-Optical Studies of Some Narrow-Gap Semiconductors	S.H. Groves	Seminar, Thomas J. Watson Research Center, Yorktown Heights, New York, 23 May 1968
2166A	Electronic Raman Scattering from Impurities in Semiconductors	G.B. Wright A. Mooradian	9th International Conference on the Physics of Semiconductors, Moscow, 23 – 29 July 1968
2182	Fourier Expansion for the Deformation Potential in the Diamond Lattice	G.F. Dresselhaus M.S. Dresselhaus	
2183	Interband Magnetoreflection of Gray Tin	S.H. Groves C.R. Pidgeon† A.W. Ewald† R.J. Wagner†	
2188	Electroreflection Study of Inversion Asymmetry and Warping Induced Interband Magneto-Optical Transitions in InSb	C.R. Pidgeon† S.H. Groves	

* Titles of Meeting Speeches are listed for information only. No copies are available for distribution.

† Author not at Lincoln Laboratory.

MS No.			
2195	An Exciton in a High Magnetic Field – Germanium	E. J. Johnson	9th International Conference on the Physics of Semiconductors, Moscow, 23 – 29 July 1968
2291	Fourier Expansions for Dispersion Relations in Semiconductors	G. F. Dresselhaus	
2210A	Finite Temperature Single-Determinant Theory	T. A. Kaplan	Seminar, Purdue University, 17 May 1968
2216	Thermal Blooming and Instability of Light Beams Due to Absorption	N. M. Kroll* P. L. Kelley	
2219	New Experimental Features of Thermal Defocusing of Laser Light in Liquids	R. L. Carman P. L. Kelley	
2221	Influence of the Molecular Interaction on the AC Kerr Effect: Possibility of a Field-Induced Phase Transition	J. Hanus	International Quantum Electronics Conference, Miami, Florida, 14 – 17 May 1968
2222	The Evolution of Intense Quasi-Monochromatic Light Pulses in Dispersive Nonlinear Optical Media	T. K. Gustafson* H. A. Haus* J-P. Taran* P. L. Kelley	
2262	Self-Steepening and Spectral Broadening of Intense Laser Light	P. L. Kelley	
2216A	Thermal Blooming and Instability of Light Beams Due to Absorption	P. L. Kelley	Seminar, United Aircraft Corporation, Hartford, Connecticut, 27 May 1968
2261A	d-Bands in Transition Metals and Oxides	J. Feinleib	Seminar, University of Chicago, 4 June 1968
2304	Laser Action and Photodetection in Lead-Tin Chalcogenides	I. Melngailis	International Colloquium on IV-VI Compounds, Paris, 15 – 18 July 1968
2349	Deviations from Stoichiometry and Lattice Defects in IV-VI Compounds and Their Alloys	A. J. Strauss R. F. Brebrick	
2307	Diffusion and Convection in Vapor Crystal Growth	T. B. Reed W. J. LaFleur A. J. Strauss	International Conference on Crystal Growth, Birmingham, England, 15 – 19 July 1968
2310	Long-Wavelength Infrared Diode Lasers of Bismuth-Doped $Pb_{1-x}Sn_xTe$	J. F. Butler T. C. Harman	Solid State Device Research Conference, University of Colorado, 17 – 19 June 1968

* Author not at Lincoln Laboratory.

Reports

MS No.			
2317	Photoresponse of $Pb_{1-x}Sn_xTe$ Detectors	A. R. Calawa I. Melngailis T. C. Harman	Solid State Device Research Conference, University of Colorado, 17 – 19 June 1968
2318	Isolation of Junction Devices in GaAs Using Proton Radiation Damage	A. G. Foyt W. T. Lindley J. P. Donnelly C. M. Wolfe	
2319	GaAs Schottky Barrier Photodiode with High Gain	W. T. Lindley R. J. Phelan, Jr. C. M. Wolfe	
2320	Far Infrared Photoconductivity in High Purity Epitaxial GaAs	G. E. Stillman C. M. Wolfe I. Melngailis C. D. Parker P. E. Tannenwald J. O. Dimmock	
2322A	Optical Heterodyne Detection of the Beat Frequency Between a Tunable Diode Laser and a CO_2 Laser	E. D. Hinkley	Seminar, M.I.T., 9 July 1968
2324	Polarons in Indium Antimonide	D. M. Larsen	Seminar, Northeastern University, 7 May 1968
2336	Light Scattering from Plasma Waves in Solids	A. L. McWhorter	International Advanced Summer Physics Institute, Chania, Crete, Greece, 1 – 12 July 1968
2337	Comparison of the Theoretical O^{--} Form Factors with Experiment	P. M. Raccah R. J. Arnott	
2338	Meaning of an Anomaly in the X-Ray Scattering of ZnSe	P. M. Raccah R. J. Arnott A. Wold*	
2339	Band Approach to the Transition Metal Oxides	J. Feinleib	
2342	Spherical Model as the Limit of Infinite Spin Dimensionality	H. E. Stanley	Banff Seminar on Critical Phenomena, Banff, Canada, 11 – 30 August 1968
2347	Exciton and Polaron Structure in the Fundamental Absorption of Semiconductors	E. J. Johnson	Seminar, General Motors Corporation, Warren, Michigan, 14 June 1968

* Author not at Lincoln Laboratory.

I. SOLID STATE DEVICE RESEARCH

A. MODULATION OF FAR-INFRARED RADIATION BY IMPACT IONIZED FREE CARRIERS IN GERMANIUM

We have utilized the free carrier absorption in n-type germanium to modulate infrared radiation in the wavelength region between 300 and 1000 μ. Fast (<0.1 μsec) pulse modulation of the free carrier absorption was achieved by impact ionization of the carriers from an impurity level to the conduction band at low temperatures by application of a pulsed electric field. The germanium crystal used in the preliminary experiments was antimony-doped n-type with a room temperature resistivity of 3 ohm-cm and a carrier concentration of 5×10^{14} cm^{-3}. The samples were in the form of 1 mm thick 4 × 4 mm square wafers. Surface damage was removed by etching with CP4 and ohmic contacts were made to opposite edges of the wafer by covering the entire 1 × 4 mm surfaces with indium solder. The sample was then mounted in a circular silvered stainless steel light pipe in such a way that all the radiation reaching the InSb detector located at the end of the waveguide had to pass through the 1 mm thick wafer. The light pipe was then inserted in a liquid helium dewar so that the InSb detector was inside a solenoidal superconducting magnet. The room temperature end of the light pipe terminated in a receiving horn.

As the germanium sample is cooled to liquid helium temperature, the conduction electrons become bound to the antimony donor atoms, which have an energy level about 0.01 eV below the conduction band edge. Thus, the free carrier absorption becomes very small, and radiation whose photon energy is smaller than 0.01 eV (wavelength longer than 120 μ) can pass largely unabsorbed through the 1 mm thick sample, since it does not excite carriers from the impurity level. When an electric field of about 5 V/cm is applied, the carriers are released by impact ionization. In our samples the breakdown occurs at ~2 V and at a current of about 10^{-7} A. Following breakdown, the current increases by six orders of magnitude at a nearly constant voltage, as the number of carriers increases due to the impact ionization. In some cases the initial breakdown occurs in filaments[1] which spread out laterally as the current is increased, until donors throughout the entire sample are ionized. At this point the current-voltage characteristic of the sample becomes ohmic. An oscilloscopic trace of the current-voltage characteristic (60-Hz source) for currents at which the ohmic region has not yet been reached is shown in Fig. I-1(a). As expected, the characteristic for negative currents is very nearly the same as for positive currents. From these measurements we also find that the sample can be operated continuously up to a current of 0.15 A. A further increase in current causes severe heating of the sample.

In the pulse modulation experiments a HCN laser and a carcinotron were used as sources of 337- and 902-μ (~1 mm) radiation, respectively. The InSb detector was operated either without a magnetic field or in a field of a few thousand gauss. The response of the magnetic-field-activated InSb detector to modulated 1-mm wavelength radiation obtained with 0.1-A current pulses applied to the germanium modulator is shown in Fig. I-1(b). The time constant of about 0.1 μsec observed in the rise and fall of the pulse is limited by the InSb detector. When the detector was operated in the zero magnetic field mode, the time constant was 0.35 μsec. To our knowledge, these are the first precise measurements of the response speed of InSb detectors

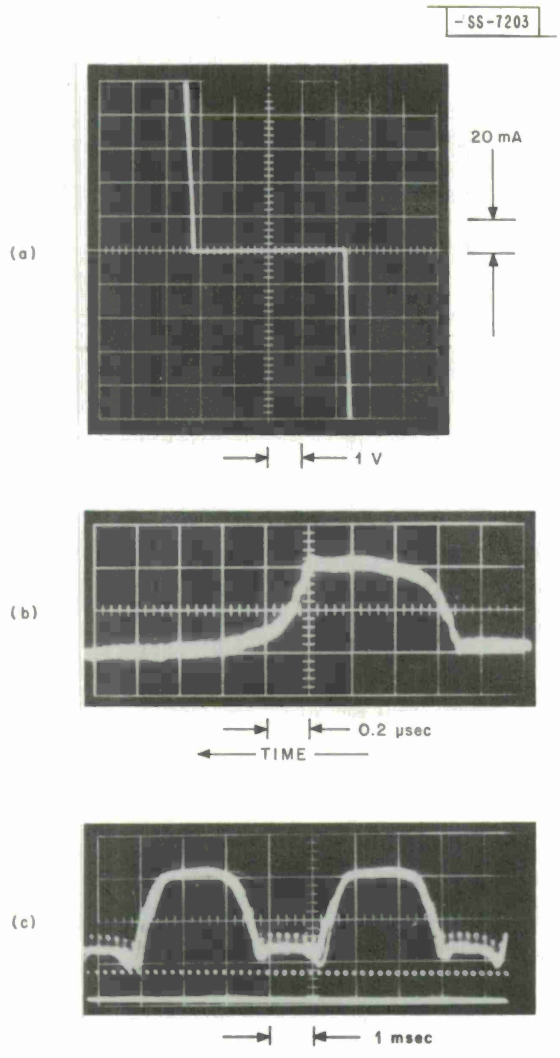

Fig. I-1. Oscilloscopic traces of characteristic current responses. (a) Current-voltage characteristic of n-type Ge sample showing forward and reverse avalanche breakdown. (b) Response of InSb detector in magnetic field of 5.5 kG. Radiation at 902 μ is being pulse-modulated by impact-ionized Ge. (c) Depth of modulation produced by Ge modulator. Upper trace shows output of InSb detector when 902-μ radiation is simultaneously chopped by mechanical wheel (235 Hz) and by Ge modulator. Lower trace shows 20-μsec current pulses applied to Ge at 5 kHz.

in this wavelength range. The response speed of the modulator is limited by the ionization and recombination times of the carriers. The ionization time, which decreases with increased driving voltage has been previously measured to be less than 10 nsec (Ref. 2). The recombination rate depends on the number of recombination sites available; hence, it decreases with increased level of ionization. In the modulators used here, the ionization time was found to be less than 10 nsec, and the recombination time, which was measured by observing the decay of conductivity in the sample following an ionizing pulse, was about 20 nsec. In compensated germanium, where a greater number of recombination sites are present, earlier work has yielded measured recombination times less than 10 nsec and predicted times as short as 0.1 nsec (Ref. 2).

The modulation depth was measured by chopping the radiation mechanically prior to its entrance into the light pipe and simultaneously pulsing the modulator. The resulting signal from the InSb detector is shown in Fig. I-1(c). By comparing the height of the series of pulses which appear during the "on" part of the chopper cycle with the amplitude of the chopper signal, we obtain a modulation depth of about 20 percent. (It should be pointed out that in the present experiment about half of the incoming radiation is reflected at the germanium surface, since no antireflection coating was provided.)

The absorption coefficient due to conduction band electrons in germanium can be estimated as

$$\alpha = 2.4 \times 10^{-12} n\lambda_o^2$$

where n is the carrier density and λ_o is the wavelength of the radiation. Assuming complete ionization in our sample during the modulating pulse ($n = 5 \times 10^{14}\ cm^{-3}$), we obtain an absorption coefficient of $\sim 10\ cm^{-1}$ at the 902-μ wavelength; i.e., about 70 percent of the radiation should be absorbed in the 1 mm thick sample, and the modulation should be about 70 percent. The 20-percent modulation depth observed in the initial tests may be low because of incomplete or filamentary ionization in the sample. Furthermore, the modulation depth of the germanium relative to that of the simultaneously operating chopper was observed to vary considerably with adjustments which could affect the phase and intensity of the radiation at the germanium surface (e.g., changes in position of the horn at the input end of the light pipe with respect to the radiation pattern of source).

Modulation measurements were also carried out with the 337-μ radiation source. Because of the RF noise associated with the gas discharge from the laser, the modulated radiation had to be detected synchronously by means of a phase sensitive detector. There was no falloff of the frequency response of the modulator up to 150 kHz (the upper limit of the synchronous detector), and the modulation depth was estimated to be a few percent.

I. Melngailis
P. E. Tannenwald

B. EPITAXIALLY GROWN GUARD RINGS FOR GaAs DIODES

A technique is presented for fabricating guard rings for GaAs p-n junction and Schottky barrier avalanche diodes. To obtain uniform avalanche diodes, it is necessary to prevent breakdown at the edges of the diodes. Although this can be done by etching mesas, GaAs diodes fabricated in this manner often show surface leakage, deterioration with time, or even complete failure at the surface. Even when the diodes are hermetically sealed in an inert atmosphere or the surfaces are coated with pyrolytic silicon dioxide or silicon nitride, these problems are not completely eliminated. Edge breakdown has been prevented in silicon devices by using diffused guard ring structures.[3] To avoid the problems involved in diffusing guard rings in GaAs, we have developed a method for growing guard rings in an epitaxial reactor in a way which is compatible with current GaAs epitaxial technology.

These epitaxially grown guard rings have been used for both p-n junction and Schottky barrier diodes[4] on ⟨100⟩ orientated GaAs. The two diode configurations are shown in Figs. I-2(a-b). For the Schottky barrier diode the Au or other high work function metal must extend out over the n^- regions. In this guard ring structure, edge breakdown is suppressed by utilizing two diodes in parallel: an annular outer diode of lightly doped material (guard ring) and an inner diode of heavier doped material (diode). Since the same voltage is applied across both diodes, the heavier doped inner diode breaks down first in reverse bias, and the space charge region of the annular guard ring isolates the junction interface of the inner diode. Because the annular guard ring has a smaller area, the outer diode does not contribute significantly to the reverse leakage current.

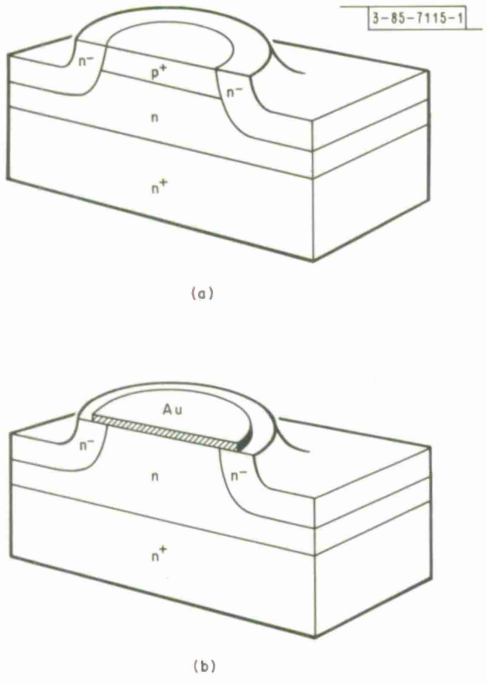

Fig. I-2. Guard ring structures for (a) p-n junction diode and (b) Schottky barrier diode. For Schottky barrier diode, the Au must extend out over the n^- regions.

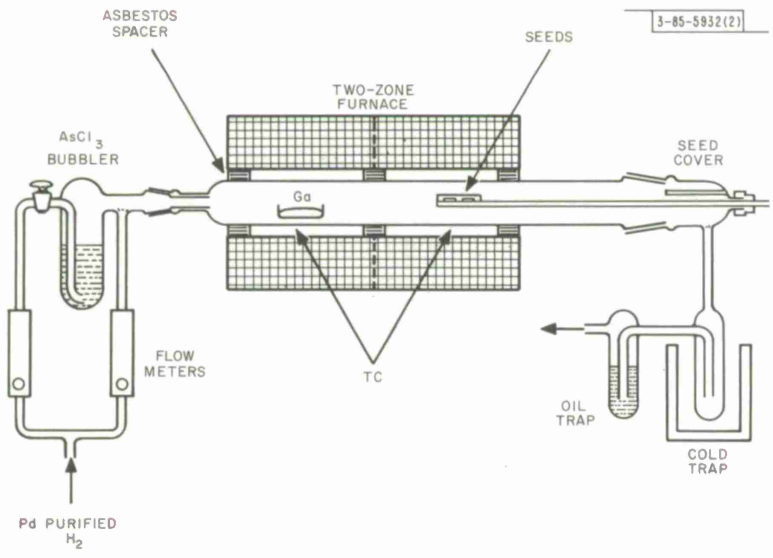

Fig. I-3. GaAs epitaxial reactor using $AsCl_3$-Ga-H_2 flow system. Two H_2 lines are used on input to vary $AsCl_3$-to-H_2 ratio. During furnace heat-up and cool-down and Ga saturation time, seeds are kept out of furnace under seed cover. Seeds are inserted or removed from furnace through air-tight Teflon coupling. Oil trap isolates system from atmosphere.

The mesas for these diodes are etched and the guard rings are grown in an epitaxial reactor utilizing the $AsCl_3$-Ga-H_2 flow system[5] by a technique previously described.[6] A diagram of the epitaxial reactor is shown in Fig. I-3. With this system the mesa etching can be carried out in a high-purity gaseous ambient and relatively uncompensated GaAs guard rings with doping levels in the 10^{14} to 10^{15} cm^{-3} range can be grown. Higher resistivity, more heavily compensated n-type material can be obtained by introducing trace amounts of O_2 into the reactor during growth.

The process used for making the guard rings around p-n junctions is illustrated in Figs. I-4(a-d). Figure I-4(a) shows the initial p^+-n-n^+ layer structure with an etch mask consisting of an array of SiO_2 disks on the p^+ region and a layer of SiO_2 on the n^+ region. The layer structure is produced by growing an epitaxial n-type layer (10^{15} to 10^{17} cm^{-3}) on an n^+ substrate ($\sim 10^{18}$ cm^{-3}) and then either diffusing Zn into the n layer or growing a Zn-doped ($\sim 10^{19}$ cm^{-3}) epitaxial layer on the n region. The SiO_2 is then deposited on both sides of the epitaxial structure by the pyrolytic decomposition of SiH_4 in the presence of O_2 at 300 °C. Islands of SiO_2 are defined by standard photolithographic techniques. To prevent severe undercutting during the subsequent high temperature furnace etching, there must be good adherence between the SiO_2 and the p^+ layer. This can be attained by ensuring a clean and oxide-free GaAs surface before SiO_2 deposition. Circles of SiO_2 as small as 2 mils in diameter on ⟨100⟩ orientated material

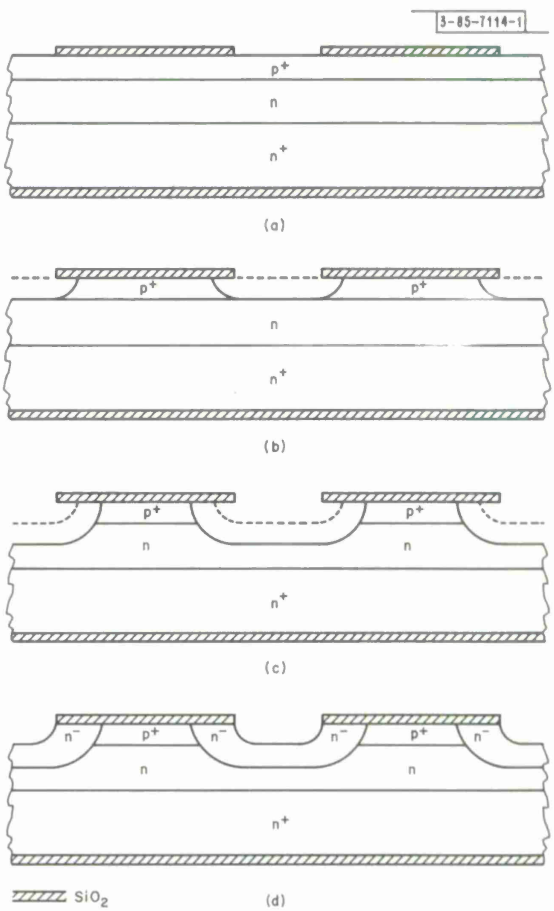

Fig. I-4. Guard ring fabrication process for p-n junction diodes. (a) Initial p^+-n-n^+ layer structure with etch mask of SiO_2 disks on p^+ region and layer of SiO_2 on n^+ region. (b) Removal of excess p^+ layer before insertion in furnace to avoid contamination of epitaxial reactor. (c) High-temperature furnace etching step to ensure clean mesa surfaces. (d) Growth of lightly doped guard rings over etched mesas.

have been cycled from room temperature to 900°C to room temperature with no loss of adherence. The n^+ side of the wafer must be coated with SiO_2 to reduce autodoping of the initial growth. When the n^+ side of the wafer is not coated with SiO_2, the resulting diodes exhibit premature reverse breakdown which is characteristic of a heavily doped region at the $n\text{-}n^-$ interface.

Before inserting the layer structure into the epitaxial reactor, the excess p^+ layer is removed [Fig. I-4(b)]. A solution of $5H_2SO_4\text{-}1H_2O_2\text{-}1H_2O$, allowed to cool for about five minutes before use, can be used to controllably remove p^+ layers several microns thick. This step in the process is necessary to avoid reactor contamination from the heavily doped p^+ layer. When the excess p^+ layer is removed by high temperature furnace etching, it is difficult to obtain lightly doped n-type material for the guard rings in the growth step. For the Schottky barrier diode configuration this pre-etch is not necessary.

To ensure a clean $n\text{-}n^-$ interface, the exposed mesas of the layer structure are re-etched in the high-purity atmosphere of the epitaxial reactor [Fig. I-4(c)]. This step is performed by inserting the layer structure in a flat temperature region of the furnace at a temperature somewhat higher than that used for growth. After thermal equilibration, the flow of H_2 through the $AsCl_3$ is started and the furnace is allowed to cool to the growth temperature. Etching occurs during the cooling of the furnace. The conditions we have used to obtain etch depths from 1 to 5 microns are listed in Table I-1. Larger amounts can be removed by initiating the etch cycle at higher temperatures. Etch conditions, however, will vary from one system to the next due in part to differences in furnace cooling rates. We have found that at an etching temperature of 800°C, compared to higher temperature etching, the etch depth is very temperature dependent. Thus good temperature control is required to reproducibly remove small amounts of material. This furnace etching process undercuts the SiO_2 at about the same rate that it etches into the sample. Caution must also be taken to avoid etching through to the n^+ layer. When this occurs, the resulting diodes exhibit premature breakdown due to autodoping of the $n\text{-}n^-$ interface.

In the next step [Fig. I-4(d)] the n^- guard ring is grown over the etched mesas. The growth of lightly doped n^- material in this system has previously been discussed in some detail.[5,6,7]

TABLE I-1
ETCHING CONDITIONS FOR {100} SEEDS

H_2 Flow through $AsCl_3$	100 ml/min
H_2 Dilution Flow	150 ml/min
Gallium Temperature	850°C
Etching Temperature	800 ± 2°C
Growth Temperature	750°C
Furnace Thermal Time Constant	~200 min
or Average Cooling Rate (800° to 750°C)	5°C/min

Growth must be obtained by a surface catalyzed reaction to prevent nucleation of the GaAs on the SiO_2. Unlike the small area {100} growth through holes in an oxide,[8] where it is difficult to terminate growth before the oxide is overgrown, this essentially large area {100} growth is sufficiently slow to make growth termination noncritical. The requirements on the doping level of the n^- guard ring are also not critical. We have found that it is only necessary that the doping level of the n^- guard ring be about a factor of five below that of the doping level of the n region of the diode. The approximate doping level of the guard ring is determined from Hall measurements on layers simultaneously grown on high-resistivity substrates.

Schottky barrier diodes with the structure which was shown in Fig. I-2(b) have been fabricated by electroplating a transparent gold film (~100 Å) onto the active diode area and over part of the epitaxially grown guard ring. By looking at the visible light emission[9] from these diodes when they are biased into reverse breakdown, the uniformity of the avalanche breakdown can be observed. For diodes fabricated on this same material with no guard ring, the breakdown light emission is entirely at the perimeter. Figure I-5 shows the light emission from one diode of an array of 3.5 mil diameter diodes which have epitaxial guard rings. The breakdown voltage of these diodes is higher than those without a guard ring and the breakdown is entirely in the center active region. The slight nonuniformity in the light emission is due to material inhomogeneity. These diodes have also been used as avalanche photodetectors and show a gain in excess of 100 when biased near their reverse breakdown.

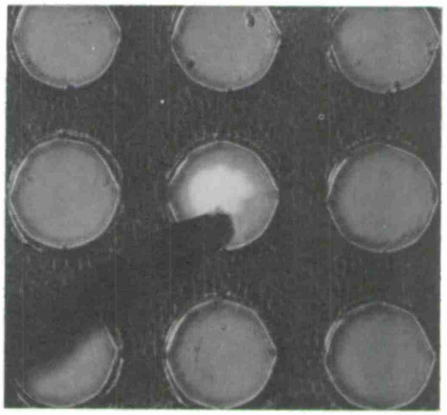

Fig. I-5. Array of 3.5-mil-diameter transparent Au-GaAs Schottky barrier diodes with epitaxial guard rings. Reverse bias visible light emission pattern is shown for center diode.

We believe that this epitaxial process for the formation of GaAs guard rings provides a useful and efficient technique for eliminating surface problems and suppressing edge breakdown in GaAs p-n junction and Schottky barrier avalanche diodes.

C. M. Wolfe
W. T. Lindley

C. CHARACTERISTICS OF InSb-MOS DETECTORS

In the past quarter we have continued the examination of InSb-metal-oxide-semiconductor (MOS) devices in order to further understand both the operation of InSb-MOS photodetectors[10] and the mechanisms involved in the imaging and storage phenomena[11] observed in these devices. The devices were fabricated[10] by anodizing the InSb to form an oxide layer about 500 Å thick on the surface. Following this a nickel film about 100 Å thick was evaporated onto the oxide. Electrical contact was made to the nickel film and to the bulk InSb. The radiation is incident on the InSb through the nickel film and oxide layer. It was initially determined[10] that the long wavelength zero bias photoresponse at 77 °K for wavelength greater than about 2 μ was due to the

generation of electron-hole pairs in a depletion region of the n-type InSb at the InSb-oxide interface. No corresponding photoresponse was observed in p-type InSb. This indicated that under the experimental conditions employed, the energy bands in the n-type InSb were bent upward at the interface giving a depletion layer, and that in p-type InSb they were either bent upward giving an accumulation layer or were flat. This model was also consistent with the observed sign of the photovoltage in n-type InSb devices. It was determined later,[11] however, that if the devices were cooled in the dark, no long wavelength photoresponse occurs in n-type InSb-MOS devices unless they are first illuminated with shorter wavelength light. On the other hand, p-type devices cooled in the dark initially showed a long wavelength response which was diminished or eliminated by shorter wavelength illumination. These results are consistent with previous measurements[12,13] which indicate that the surface of p-type InSb can be changed from an n-type inversion layer to a p-type accumulation layer by illumination.

In order to develop a precise model for these effects, we have measured the unbiased DC photovoltaic response[14] of n-type InSb-MOS detectors over the spectral range from 5 to 0.25 μ at room temperature, 195 °K and at 77 °K and the DC photocurrent at room temperature and 77 °K as a function of bias. In addition, we have measured the photoresponse of the n-type InSb at 77 °K to modulated radiation at 3.9 μ from an InAs diode.[15] This response has now been observed both as a function of applied bias and of short wavelength light incident on the devices. As mentioned previously,[15] in our model of the MOS structure, this long wavelength radiation acts as a probe of the InSb depletion region and has no other effect on the state of the devices. Measurements of the depletion region should, in turn, give an indication of the charge state of the oxide and of the interface. The model which is emerging from the measurements consists of the following:

(1) At long wavelengths the light penetrates the nickel and oxide layers and generates electron and hole pairs in the InSb (long wavelength response limit at 77 °K is 5.4 μ, corresponding to the bandgap of InSb). In general for photon energies less than 0.5 eV, the electron-hole pairs remain in the InSb and do not otherwise alter the system.

(2) For photon energies between 0.5 and 2.0 eV, depending on the initial state of the system, some of the photoexcited electrons in the InSb can enter the oxide and become trapped there or at the interface. This appears to occur under those conditions in which there is a field in the oxide due to previous charging, which tends to lower the effective electron barrier between the InSb and the oxide allowing photoexcited electrons of low energy to either pass over or tunnel through the barrier. Under these conditions the photoexcited electrons can affect the charge state of the oxide which changes the response of the n-type InSb to the 3.9-μ InAs diode radiation. When the oxide has not been charged previously and either no bias or a positive bias is applied to the InSb, photoexcited electrons in this energy range are prevented from entering the oxide by the barrier at the interface.

(3) At photon energies greater than about 2.0 eV, photoexcited electrons in the InSb are emitted into the oxide and become trapped there regardless of the initial state of the system.

(4) The presence of trapped negative charge in the oxide or at the InSb-oxide interface produces an electric field at the surface of the InSb such that a depletion region is created in n-type InSb. This can also be accomplished, in the absence of trapped charge, by applying a positive bias to the InSb. If the amount of trapped charge becomes sufficiently large an inversion layer is formed and under these conditions the application of additional

positive or negative bias to the InSb does not significantly alter the depletion region or affect the response to the 3.9-μ InAs diode radiation. This response will presumably be zero for no depletion region and a maximum when the depletion region is fully formed but little or no region of inversion present.

(5) At photon energies in excess of about 3.0 eV, the oxide becomes photoconductive. The photoconductivity reaches a peak at about 3.9 eV and decreases somewhat at higher energies. At these high photon energies, electrons are still being photoemitted from the InSb into the oxide. Depending on the applied bias, these electrons will either be conducted through the oxide (InSb biased negative) or accumulated and partially trapped at or near the InSb-oxide interface (zero bias or InSb biased positive). Under these conditions regardless of the bias applied, the amount of trapped charge in the oxide never gets sufficiently large to create an inversion region, since the response to the InAs radiation can still be changed by the application of additional bias. In the energy region between 3.0 and 4.5 eV, there is a competition between the photoemission and photoconductivity effects which is influenced in addition by external bias. The effects, however, are distinct and have been resolved.

(6) Both the trapped charge in the oxide or at the interface and the light induced photoconductivity can have long lifetimes and the effects of both may persist for some time. The response to the InAs radiation changes very little with time if the MOS detector is kept in the dark at 77 °K and, in fact, decreases only by about a factor of two if the detector is kept in the dark overnight at room temperature. Direct measurements of the dark resistance of the oxide after exposure to light of various photon energies show changes of long duration.

At room temperature there are a large number of thermally generated electrons and holes in the InSb such that there is virtually no depletion region as evidenced by the absence of appreciable long wavelength photoresponse in either n- or p-type devices. In this case all photovoltaic and photoconductive responses are due to effects occurring in the oxide. The photovoltaic response at low photon energies is due to the emission of photoexcited electrons from the InSb into the oxide. At higher photon energies, the oxide becomes photoconductive. In the uncharged state the photovoltaic threshold is at about 1.4 eV, whereas appreciable photoconductivity does not appear until nearly 3.0 eV. However, in the charged state the low energy photovoltaic response is increased and the threshold is reduced to about 1.2 eV. In this state the photoconductivity rises abruptly at about 1.2 eV and continues to beyond 4.0 eV. This is probably due to the fact that photoexcited electrons are emitted from the InSb into the oxide and that other electrons trapped in the oxide are released from the traps by relatively low energy photons. At low temperatures there may be an accumulation or a depletion region in the InSb, depending on the amount and sign of the charge trapped in the oxide and at the interface. If there is no trapped charge in the oxide, the energy bands in the InSb bend down at the interface giving an accumulation region in n-type InSb and a depletion region in p-type InSb. As electrons are transferred from the InSb to the oxide and become trapped there, the resultant field causes the bands to bend upward creating a depletion region in n-type InSb and an accumulation region in p-type InSb. Further transfer of negative charge can cause an inversion layer at the surface of n-type InSb. This is reflected in the response of the InSb MOS detector to the 3.9-μ InAs diode radiation and appears to be a controlling factor in the performance of the device.

W. E. Krag
R. J. Phelan, Jr.
J. O. Dimmock

D. HIGH RESISTIVITY LAYERS PRODUCED IN ZnTe BY PROTON BOMBARDMENT

It has recently been shown that proton radiation can produce high resistivity layers in GaAs and that this technique is potentially useful in the isolation of devices and the fabrication of arrays.[16] In this report we will present some initial proton radiation experiments on ZnTe.

The ZnTe crystals, which were not intentionally doped, had a carrier concentration of $2 \times 10^{16}\ cm^{-3}$ and a room temperature mobility of $77\ cm^2/Vsec$. Following standard polishing and etching procedures, an array of thin gold contacts (15 mil squares on 20 mil centers) was electroplated on the front surface of each sample. These contacts were thin enough (~500 Å) so that they had negligible effect on the penetration of the proton beam into the sample. A single large gold contact was plated on the back of each sample. Before bombardment, all the contacts were ohmic with a contact-to-contact resistance of approximately 200 ohms.

Using a 400-kV Van de Graaff generator, the front surface of each sample was bombarded with a $0.1\text{-}\mu A/cm^2$, 400-kV proton beam for 200 sec, giving a total dose of approximately 10^{14} protons/cm^2. After bombardment the current – voltage characteristics between adjacent contacts on the front surface showed a resistance greater than 10^9 ohms in either direction out to 120 V where sharp breakdown occurred. Between a gold contact on the front surface and the large back contact, a resistance greater than 10^9 ohms was again observed with breakdown occurring at 90 volts with the top gold contact biased positively and at 40 V with this contact negative. These current-voltage characteristics and some preliminary capacitance measurements indicate that the 400-keV proton beam has created a high resistance layer in the ZnTe approximately 4 μ deep.

Further experiments are being carried out to determine the range of protons vs energy, carrier concentration profiles and other electrical characteristics.

J. P. Donnelly
A. G. Foyt
W. T. Lindley

E. METAL INCLUSIONS AND CELLULAR SUBSTRUCTURE IN $Pb_{1-x}Sn_xTe$ SINGLE CRYSTALS

The study of metal inclusions and low angle grain boundaries in $Pb_{1-x}Sn_xTe$ crystals has been continued using the techniques previously described.[17] A large number of Bridgman- and vapor-grown crystals has been examined and it is now possible to correlate the presence or absence of these macroscopic defects with growth conditions. Table I-2 indicates the presence or absence of metallic inclusions and cellular substructure in several crystals of $Pb_{0.8}Sn_{0.2}Te$. Bulk metal inclusions, when present, varied in number from essentially zero at the first end to freeze to a maximum at the opposite end of each crystal. The density of inclusions decreased as the composition was shifted to the Te-rich side. Surface inclusions were distributed rather uniformly over the exterior surfaces of the crystals. A second $M_{0.49}Te_{0.51}$ crystal was grown which was free of both bulk and surface inclusions. The inner surface of the silica growth ampoule for this crystal had been carbonized by the reduction of acetone, whereas the former crystal was grown in an ampoule carbonized by the reduction of natural gas. This result indicates that surface inclusions may be due in part to a chemical reaction of $Pb_{1-x}Sn_xTe$ with the surface of the silica growth tube and can be minimized. When present at all, the cellular

TABLE I-2

OCCURRENCE OF METALLIC INCLUSIONS AND CELLULAR SUBSTRUCTURE IN CRYSTALS OF $Pb_{0.8}Sn_{0.2}Te$

	Liquid Composition	Bulk Inclusions	Surface Inclusions	Low-Angle Grain Boundaries
Bridgman Technique	$M_{0.506}Te_{0.494}$	Present	Present	Present
	$M_{0.500}Te_{0.500}$	Present	Present	Present
	$M_{0.496}Te_{0.504}$	Present	Present	Present
	$M_{0.493}Te_{0.507}$	Present	Present	Present
	$M_{0.49}Te_{0.51}$	Absent	Present*	Absent
	$M_{0.49}Te_{0.51}$	Absent	Absent*	Absent
	Source Composition			
Vapor-Growth Technique	$M_{0.51}Te_{0.49}$	Absent	Present	Absent

* See text.

substructure was found throughout the crystal. A number of the vapor-grown crystals were etched by the technique previously described. No evidence for the presence of either metal inclusions or cellular substructure was found in the bulk of these crystals. However, metal inclusions in the surface layers of crystals vapor grown from metal-rich sources were observed for all crystals. In the case of crystals vapor grown from a Te-rich source, no metal inclusions were evident in the surface layers directly exposed to the vapor. However, even in this latter case, inclusions were seen on surfaces in contact with the inner walls of the quartz growth capsule.

We believe the bulk metal inclusions and cellular substructure are due to constitutional supercooling during growth. The mechanism of constitutional supercooling has been previously used to explain cellular growth and other defects in various crystals.[18] In our model, it is caused by the difference between the metal-Te ratio in the melt and solid of a growing crystal. This is illustrated in Figs. I-6 and I-7(a-b). Figure I-6 shows an idealized equilibrium phase diagram for $Pb_{1-x}Sn_xTe$ near the stoichiometric composition. For $x = 0.2$, the maximum melting temperature is approximately 890°C, and intersection of the solidus line with the stoichiometric line occurs at about 525°C. Figure I-7(a) shows schematically how the metal-Te ratio varies across the interface between the melt and solid of a growing crystal. The buildup of the metal-to-tellurium ratio in the liquid at the interface depends on the growth rate and would be absent for an infinitesimally slow rate. The pertinent compositions are shown at the liquidus

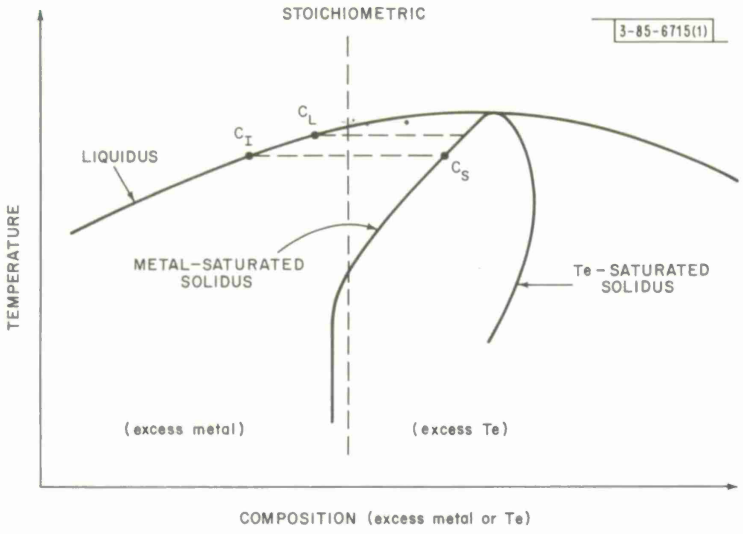

Fig. I-6. Schematic of equilibrium phase diagram of $Pb_{1-x}Sn_xTe$ near the stoichiometric composition.

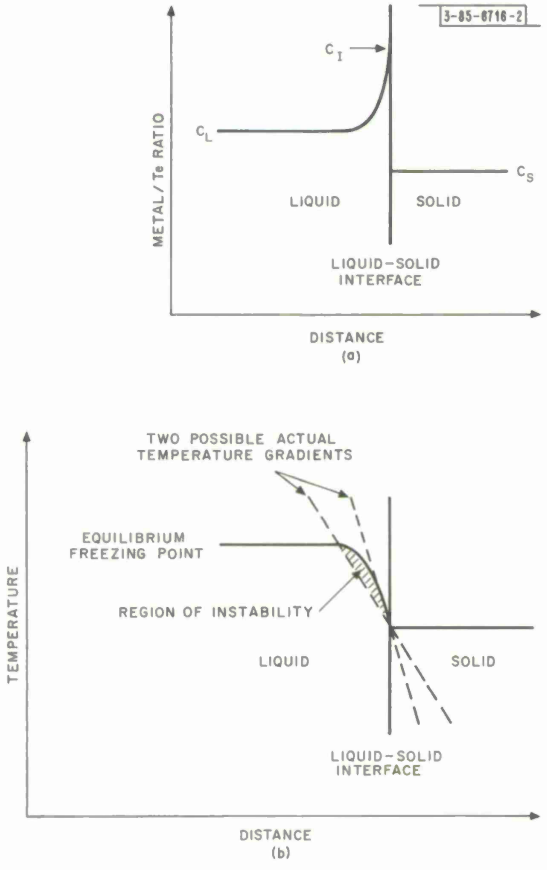

Fig. I-7. (a) Schematic of metal/Te ratio near freezing interface of growing crystal of $Pb_{1-x}Sn_xTe$. C_L, C_I and C_S are metal/Te ratios in the liquid far from the interface, in the liquid at the interface and in the solid, respectively. (b) Schematic of equilibrium freezing temperature variation near freezing interface along with two possible gradients of actual temperature and region of instability.

and solidus temperatures in Fig. I-6. It is evident that the equilibrium freezing temperature in the liquid will vary with position as a result of the varying metal/Te ratio. The variation of freezing temperature is shown schematically in Fig. I-7(b). Also shown are two possible actual temperature gradients. For the less steep line there is a region of instability where liquid is locally supercooled. Rapid quenching will occur in this region causing spurious nucleation and leading to cellular substructure. In addition, the rapidly quenched solid material should contain metal-rich liquid as a second phase at the higher temperatures and two solid phases at lower temperatures: $Pb_{1-x}Sn_xTe$ and metal.

This qualitative explanation for the macroscopic defects suggests some practical methods of avoiding them. As may be seen from Fig. I-6, C_I, C_L and C_S should be identical at the maximum melting point composition; hence, growth from a liquid of this composition will eliminate constitutional supercooling. Crystal growth from a melt composition richer in Te than the maximum melting point composition should also yield crystals free of metal inclusions. We believe the $M_{0.49}Te_{0.51}$ crystals mentioned previously were grown from a melt at approximately the maximum melting point composition. These were free of bulk metal inclusions and cellular substructure. According to Fig. I-7(b) constitutional supercooling can also be prevented by imposing a steep enough temperature gradient or by reducing the slope of the freezing temperature curve by decreasing the growth rate.

J. F. Butler
T. C. Harman

F. BISMUTH DOPED $Pb_{1-x}Sn_xTe$ DIODE LASERS

The wavelength of diode laser emission in the PbTe rich side of the $Pb_{1-x}Sn_xTe$ system is increased by increasing x, the fraction of SnTe, and has so far been extended to 28 μ (Ref. 19). However, as x is increased n-type conductivity becomes difficult to achieve because of the shift of the solidus field to the Te-rich side of the equilibrium phase diagram.[20] This is illustrated schematically in Fig. I-8 which shows the metal-Te equilibrium phase diagram in the vicinity of the stoichiometric line for PbTe and for a composition of $Pb_{1-x}Sn_xTe$ near x = 0.2 With increasing x the maximum concentration of excess metal atoms and, hence, the maximum electron concentration in undoped crystals, becomes smaller. Furthermore, temperatures for annealing on the metal rich side become lower, giving rise to longer annealing times. To counteract these effects, several crystals of $Pb_{1-x}Sn_xTe$ doped with Bi, a donor impurity, were grown. The main effect of doping with Bi is believed to be a shift of the composition at which n = p to the Te-rich side of the stoichiometric line.

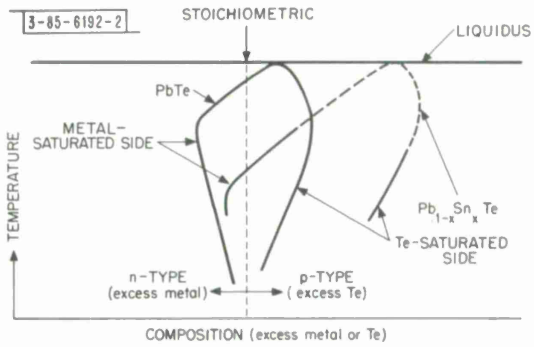

Fig. I-8. Binary equilibrium phase diagram near stoichiometric composition for two members of $Pb_{1-x}Sn_xTe$ family.

TABLE I-3

ANNEALING PARAMETERS AND THRESHOLD CURRENT DENSITIES FOR $Pb_{1-x}Sn_xTe$ DIODE LASERS

	x	Annealing Time (days)	Annealing Temperature (°C)	Minimum Threshold Current Density (A/cm^2)	
				12°K	77°K
Undoped	0.15	None	None	250	3,000
	0.17	2	450	55	10,000
	0.19	3	450	130	9,000
	0.20	3	450	275	12,500
	0.21	2	450	175	7,000
	0.22	7	450	175	
	0.24	14	400	230	
	0.27	0.17	700	125	
		6	650		
		7	450		
		21	400		
Bismuth Doped	0.245	3	450	93	3,200
	0.25	3	450	75	5,000
	0.26	4	450	71	1,400

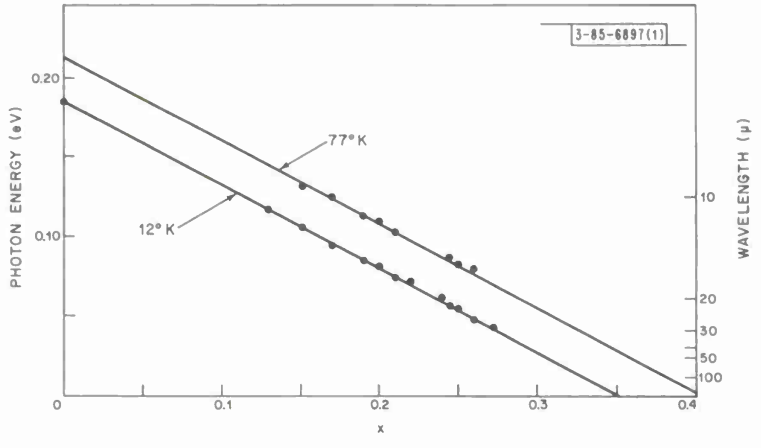

Fig. I-9. Photon energy of laser emission vs fraction of SnTe for $Pb_{1-x}Sn_xTe$.

The Bi-doped crystals were grown and isothermally annealed by the method previously described,[19] with 4×10^{19} cm^{-3} Bi atoms added to the source ingot. Diode lasers were fabricated in the usual manner and were tested at 77° and 12°K. Table I-3 shows annealing parameters for producing p-n junction depths of approximately 30 μ and threshold current densities for a number of compositions of doped and undoped crystals. As expected, annealing times become longer with increasing x but are markedly reduced by the addition of Bi. The Bi doping also causes a reduction in threshold current densities at both 12° and 77°K. This effect is most pronounced at 77°K where, in the composition range $0.24 \lesssim x \lesssim 0.27$, undoped lasers did not exhibit laser action for current densities up to 30,000 A cm^{-2}, while doped lasers had remarkably low threshold currents. Such a reduction in threshold current would be expected if the region in which recombination occurs were nondegenerate in undoped lasers and degenerate in doped lasers.

Figure I-9 shows photon energies plotted against composition for $Pb_{1-x}Sn_xTe$ lasers. This variation with x is as predicted by Dimmock, Melngailis and Strauss[21] and the existence of laser action is evidence that the bandgap is direct to at least $x = 0.27$.

J. F. Butler
T. C. Harman

REFERENCES

1. I. Melngailis and A. G. Milnes, Appl. Phys. 33, 995 (1962).
2. A. L. McWhorter and R. H. Rediker, Proc. IRE 47, 1209 (1959).
3. R. L. Batdorf, A. G. Chynoweth, G. C. Dacey and P. W. Foy, J. Appl. Phys. 31, 1153 (1960); A. Goetzberger, B. McDonald, R. H. Haitz and R. M. Scarlett, J. Appl. Phys. 34, 1591 (1963).
4. W. T. Lindley, R. J. Phelan, Jr. and C. M. Wolfe, IEEE Solid-State Device Research Conference, Boulder, 17 – 19 June 1968.
5. J. R. Knight, D. Effer and P. R. Evans, Solid State Electron. 8, 178 (1965); D. Effer, J. Electrochem. Soc. 112, 1020 (1965).
6. C. M. Wolfe, A. G. Foyt and W. T. Lindley, Electrochem. Tech. 6, 208 (1968).
7. E. W. Mehal and G. R. Cronin, Electrochem. Tech. 4, 540 (1966); D. E. Bolger, J. Franks, J. Gordon and J. Whitaker, Proceedings of the International Symposium on Gallium Arsenide, Reading, 1966 (Institute of Physics and The Physical Society, London, 1967), p. 16; M. Maruyama, S. Kikuchi and F. Hasegawa, Electrochemical Society Meeting, Boston, 5 – 9 May 1968 (Abstract No. 62).
8. D. W. Shaw, J. Electrochem. Soc. 113, 904 (1966).
9. A. E. Michel, M. I. Nathan and J. C. Marinace, J. Appl. Phys. 35, 354 (1964).
10. R. J. Phelan, Jr. and J. O. Dimmock, Appl. Phys. Letters 10, 55 (1967).
11. R. J. Phelan, Jr. and J. O. Dimmock, Appl. Phys. Letters 11, 359 (1967).
12. R. K. Mueller and R. L. Jacobson, J. Appl. Phys. 35, 1521 (1964).
13. G. K. Eaton, R. E. J. King, F. D. Morton, A. T. Partridge and J. G. Smith, J. Phys. Chem. Solids 23, 1473 (1962).
14. Solid State Research Report, Lincoln Laboratory, M.I.T. (1968:1), p. 3.
15. Op. cit. (1968:2), p. 11.
16. Ibid., p. 10.
17. J. F. Butler and T. C. Harman, Solid State Research Report, Lincoln Laboratory, M.I.T. (1967:4), p. 5.
18. See, for example, M. Tanenbaum in Semiconductors, N. B. Hannay, Ed. (Reinhold, New York, 1959), p. 91; and W. Bardsley, J. S. Boulton and D. T. J. Hurle, Solid State Electron. 5, 395 (1962).
19. J. F. Butler and T. C. Harman, Appl. Phys. Letters 12, 347 (1968); also, Ref. 15, p. 5.
20. A. R. Calawa, T. C. Harman, M. Finn and P. Youtz, Trans. AIME (March 1968).
21 J. O. Dimmock, I. Melngailis and A. J. Strauss, Phys. Rev. Letters 16, 1193 (1966).

II. OPTICAL TECHNIQUES AND DEVICES

A. 100-WATT CO_2 AMPLIFIER

The small signal gain has been determined for the 9-m CO_2 amplifier mentioned in previous solid state research reports.[1]

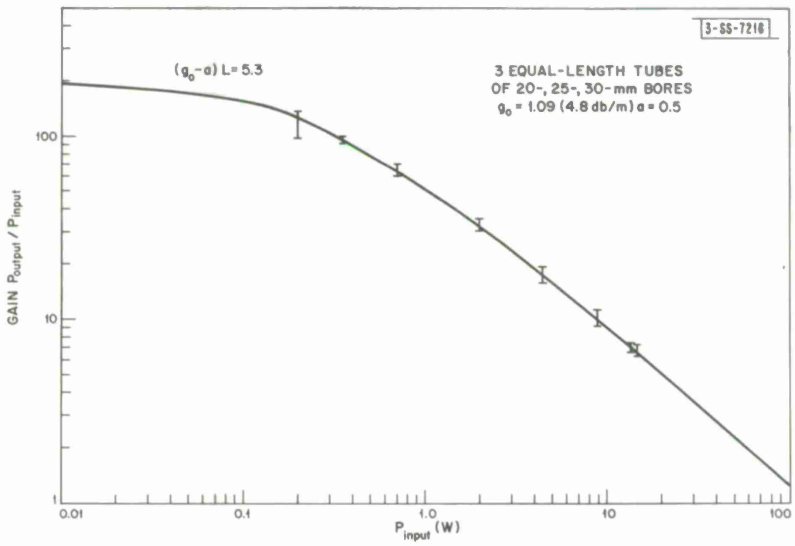

Fig. II-1. Measured gain of 9-m CO_2 amplifier with average bore of 25 mm is plotted as a function of input optical power at 10.6 μm. Analytical case assuming homogeneous line broadening and loss is drawn through data.

The gain measurements were made with the amplifier sealed off and containing a gas mixture that was varied slightly around 4 torrs He, 0.9 torr CO_2, 1.2 torrs N_2, and 0.2 torr H_2. An analytical curve shown in Fig. II-1 is drawn through the data points and is given by the homogeneous gain saturation equation with loss as

$$(g_o - a)\, L = \ln G - \left(\frac{g_o}{a}\right) \ln \left[\frac{1 - a/g_o \left(1 + G\, \frac{P_{in}}{P_s}\right)}{1 - a/g_o \left(1 + \frac{P_{in}}{P_s}\right)} \right]$$

where g_o is the zero or small signal gain, a the fractional loss in the amplifier, G the amplifier gain (power output divided by power input) and P_s the saturation parameter. The saturation intensity using the $1/e^2$ power points as the beam diameter for the TEM_{oo} mode was computed to be 49 watts/cm^2 taking an average beam radius of 0.71 cm in the amplifier. The extrapolated small signal gain taking an average tube bore of 25 mm was found to be 4.8 db/m which compared favorably with the highest gain published for flowing gas amplifiers.[2,3]

R. J. Carbone

B. OPTICAL ASPECTS OF OPTIMUM LASER HETERODYNING

The usefulness of the f-number criterion for the achievement of optimum "optical" heterodyning has been demonstrated experimentally.

Preliminary considerations of the electric field conditions which will give the best heterodyne S/N when two fields are mixed in a square-law detector indicate that the two field distributions should differ only by a multiplicative constant and that the field polarizations should be identical. The field distributions in the detector are made similar by forming similar 2-dimensional distributions on the limiting apertures of the two optical systems which are used to focus the LO and signal beams, and by making these two optical systems with the same f-number, F. The F for the Airy pattern is defined either in terms of the limiting aperture diameter, D, and system focal length, f, or in terms of the focal spot radius, r_o, and wavelength, λ,

$$F = \frac{f}{D} = \frac{r_o}{\lambda} \quad .$$

For a laser mode with a minimum waist, w_o, F is given approximately by

$$F = \sqrt{2}\,\frac{w_o}{\lambda} \quad .$$

The efficiency, $\mathcal{E}$, of various optical systems made by using the F matching criterion was determined by comparing the measured heterodyne signal power, P_a, with the expected signal power, P_e, which was determined from measurements of the LO and signal DC currents, I_{LO} and I_s, in the detector.

$$\mathcal{E} = P_a/P_e \quad .$$

$$P_e = 2I_s I_{LO} R_L \cos^2\Theta \quad ,$$

where R_L is the load and Θ is the angle between the polarizations of the two fields. $\mathcal{E}$ is proportional to the heterodyne $(S/N)_{power}$.

When two laser beams which were offset in frequency by about 4 MHz were mixed, the best $\mathcal{E}$ achieved in a Cu-doped Ge detector for directly matched laser modes was 55 percent. When one laser was used to transmit a 1-cm beam 100 m to a spherical target whose return was gathered by an F = 16.3 Cassegrainian telescope and the other laser beam was made to construct both the Airy and Gaussian matched F, $\mathcal{E}$ = 25 percent was achieved in both cases. The F match and, thus, $\mathcal{E}$, could have been improved in this last set of experiments. However, the best efficiency achieved under a variety of conditions has been about 50 percent consistently. This discrepancy from the ideal is not yet well understood.

T. J. Gilmartin
H. A. Bostick

C. ATMOSPHERIC PROPAGATION EFFECTS AT 10 μm

Some preliminary propagation measurements and calculations at 10 μm are being made in anticipation of the requirements and capabilities of the Millstone Hill CO_2 laser radar.

The geometry of the Millstone system is such that the transmitted beam passes in front of the receiver aperture several times before being transmitted. The power which is Rayleigh

scattered into the receiver during these passes has been calculated to be $10^{-21} \sin^2 \varphi$ times the transmitted power, where φ is the angle between the field polarization and receiver axis. This is negligible.

Calculations indicate that scintillation will limit the useful heterodyne receiver aperture for a wave passing vertically through the full atmosphere to a 50-cm diameter in weak turbulence and 10-cm diameter in strong turbulence. As expected, this effect was not measurable with a 20-cm aperture over a 100-m horizontal path, even through strong turbulence.

Turbulence will also cause the laser beam to be scattered and broadened. From profile measurements of the broadened beam, one can determine the intensity and scale of the turbulence. Preliminary measurements on the 100-m range have shown insufficient broadening to yield useful data.

A 1.3-km round trip range is being set up. The aperturing and beam-broadening experiments will be continued on this range with a 30-cm aperture. In addition, water vapor absorption, which can account for up to 2-db/km loss, will be measured.

T. J. Gilmartin

D. TUNABLE INFRARED LASER HETERODYNE EXPERIMENTS

Optical heterodyne detection of the beat note between a tunable $Pb_{1-x}Sn_xTe$ diode laser and the P_{20} emission line from a CO_2 gas laser was reported previously.[4] Several experiments have since been performed to learn more about the tuning mechanism of the diode laser and its heterodyne behavior. We have found, for example, that the positions of the diode laser modes can be changed by reducing the cavity size with an electrolytic etch – although substantial etching can reduce the cavity Q and produce multimoding. In these later experiments heterodyning has been performed with the P_{18} and P_{22} emission lines from the gas laser, as well as with the P_{20} line, and beat frequencies from essentially zero to 3.5 GHz measured. Stable battery operation of the diode laser has produced initial linewidth data. The frequency response of a Ge:Cu detector similar to one scheduled for use in the CO_2 Doppler radar system has also been measured.

1. Temperature Dependence of the Beat Frequency: Thermal Conductivity

Tuning of the output frequency of the infrared emission from a $Pb_{1-x}Sn_xTe$ diode laser is accomplished by changing its temperature, and, consequently, its refractive index. Because of the relatively poor thermal conductivity of this mixed-crystal semiconductor, the junction temperature may be raised fractions of a degree (more or less, depending on the diode dimensions) above the heat sink temperature by diode currents of 1 A – therefore, current tuning is actually temperature tuning. In order to deduce a value for the effective thermal conductivity of the $Pb_{0.88}Sn_{0.12}Te$ material, two heterodyne experiments were performed. In the first, the diode current was held constant and the beat frequency measured as a function of heat sink temperature, controlled and measured by two carbon resistors. The results are shown in Fig. II-2, where the slope corresponds to a temperature-tuning rate of −4.5 GHz/°K. The same type of plot is obtained when the diode current is changed and the heat sink temperature held constant, yielding, for this particular diode laser, a current-tuning rate of −40 MHz/mA. Dividing these two quantities yields $dT/dI = 8.9°K/A$.

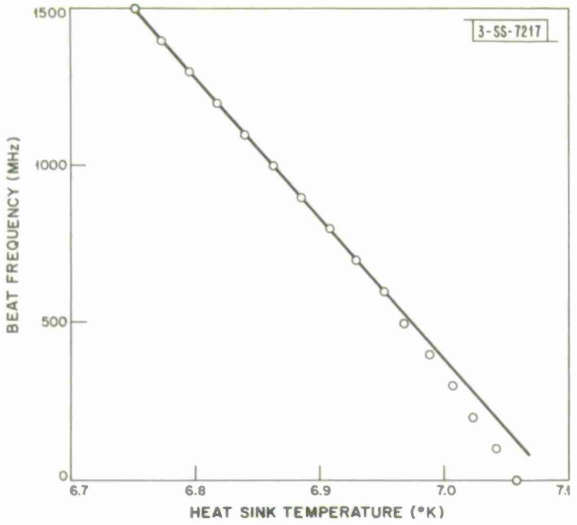

Fig. II-2. Temperature dependence of heterodyne beat frequency for fixed diode current. Thermal tuning rate is −4.5 GHz/°K. Diode laser dimensions: 0.071 cm long, 0.051 cm wide, 0.018 cm thick, with 0.004 cm deep junction.

If we assume that only the heat generated by nonradiative and absorptive processes in the junction region is significant, and that the radiated energy can be neglected, then the junction temperature is given by

$$T = T_o + IV_g d/\kappa \ell w \quad , \tag{I-1}$$

where T_o is the (constant) heat sink temperature, I the diode current, d (0.004 cm) the distance from the junction plane to the heat sink, w (0.051 cm) the diode width, ℓ (0.071 cm) the diode length, V_g (0.12 V) the junction voltage, and κ the effective thermal conductivity. Differentiating Eq. (I-1) with respect to I, and solving for κ, yields

$$\kappa = (V_g d/\ell w)\,(dT/dI)^{-1} \approx 0.02 \text{ W/cm-°K} \quad . \tag{I-2}$$

Low temperature measurements of the thermal conductivity of $Pb_{1-x}Sn_xTe$ have not been made, but rough extrapolations from room temperature data[5] indicate that this result is not unreasonable. The largest error in the above analysis is thought to stem from a neglect of Joule heating due to the series resistance of the diode laser. If this were taken into account, the deduced thermal conductivity would be somewhat larger.

In Fig. II-2 the deviation of the data points below 500 MHz from the straight line is probably caused by frequency "pulling" exerted by the CO_2 laser. Frequency "pulling" and "locking" have been observed several times during these experiments, especially near zero beat frequency; and the effect is sensitive to the precise alignment of the apparatus, which determines the amount of feedback of the CO_2 laser energy to the diode laser. Since frequency "pulling" of over 200 MHz has been observed, it is obviously the diode laser emission frequency which is being altered, rather than the CO_2 emission which has a spontaneous linewidth of only 50 MHz.

2. Current-Tuning Rate: Index of Refraction

In a laser cavity the mode separation $\Delta\nu_m$ is determined by the relation

$$\Delta\nu_m = \frac{c}{2\ell\eta} = \frac{c}{2\ell\left(\eta_o + \nu\,\frac{\partial\eta}{\partial\nu}\right)} \quad , \tag{I-3}$$

where η is the index of refraction and c is the speed of light. In Fig. II-3 is shown the wavenumber of $Pb_{0.88}Sn_{0.12}Te$ diode laser emission as a function of current; seven modes are illustrated, each representing a continuous tuning range of approximately 6 GHz. (Because of a mode "locking" effect, the tuning range within each mode is actually twice that illustrated, since these data represent only monotonically increasing values of diode current.) The unknown dispersion term $\partial\eta/\partial\nu$ in Eq. (I-3), prevents a determination of η_o from the mode spacing. Engeler and Garfinkel have shown,[6] however, that the refractive index may be deduced from a curve similar to that of Fig. II-3 by comparing the ratios of the spontaneous tuning rate (variation of energy gap with temperature) and intramode tuning rate (variation of refractive index with temperature). The dashed line of Fig. II-3 approximates the increase of the energy gap with diode current (temperature). The slope of the short solid line near the P_{20} transition corresponds to the increase of the refractive index with current (temperature). The pertinent equation may be written as

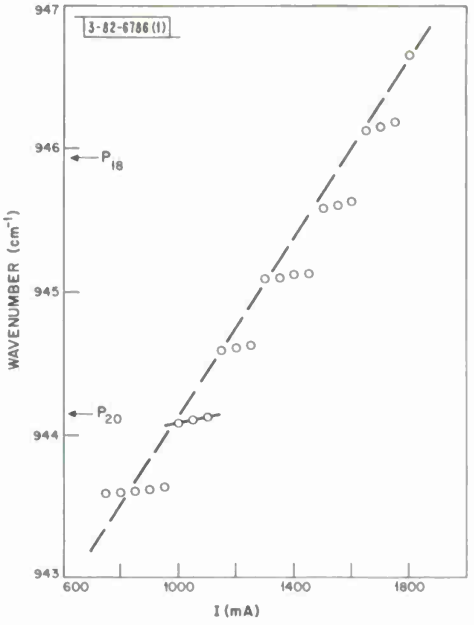

Fig. II-3. Current-tuning of 0.13 cm-long $Pb_{0.88}Sn_{0.12}Te$ diode laser at liquid helium temperature. Also indicated are the positions of the P_{18} and P_{20} emission lines of a CO_2 laser.

$$d\nu_m/dI = [(\eta - \eta_o)/\eta]\,[d\nu_{sp}/dI] \quad , \tag{I-4}$$

where the subscript m refers to intramode tuning, and sp to the spontaneous or energy-gap tuning. In this case, the cavity length is 0.13 cm and the mode separation 0.5 cm^{-1} (15 GHz), yielding η = 7.7. From Eq. (I-4), using the slope data of Fig. II-3, we obtain η_o = 6.6.

3. Tuning Speed: Current and Magnetic Field Tuning

Because current tuning of the diode laser is basically a thermal phenomenon, time constants associated with the heat capacity of the material limit the speed with which the laser frequency can follow changes in the diode current. The frequency modulation effect on the heterodyne beat note caused by 120-Hz ripple in the diode current supply was previously noted.[4] In order to analyze further the response time for diode laser tuning, a 4-mA sinusoidal current, adjustable in frequency from 50 Hz to 50 kHz, was superimposed on a steady direct current of approximately 1.5 A. Since the tuning rate for this particular diode is 12.8 MHz/mA, the total frequency spread of the beat note is slightly over 50 MHz for the 4-mA "ripple" current at low frequencies. In Fig. II-4 are shown values for the spread of the beat frequency, as measured on a spectrum analyzer, vs the frequency of the sinusoidal "ripple" current. Cutoff occurs at a few hundred hertz, corresponding to a response time of the order of 1 msec or a maximum tuning speed of 50 MHz/msec. It should be mentioned that, although band filling could also be responsible for current tuning of the $Pb_{1-x}Sn_xTe$ diode laser, the tuning speed would be much higher than that illustrated in Fig. II-4.

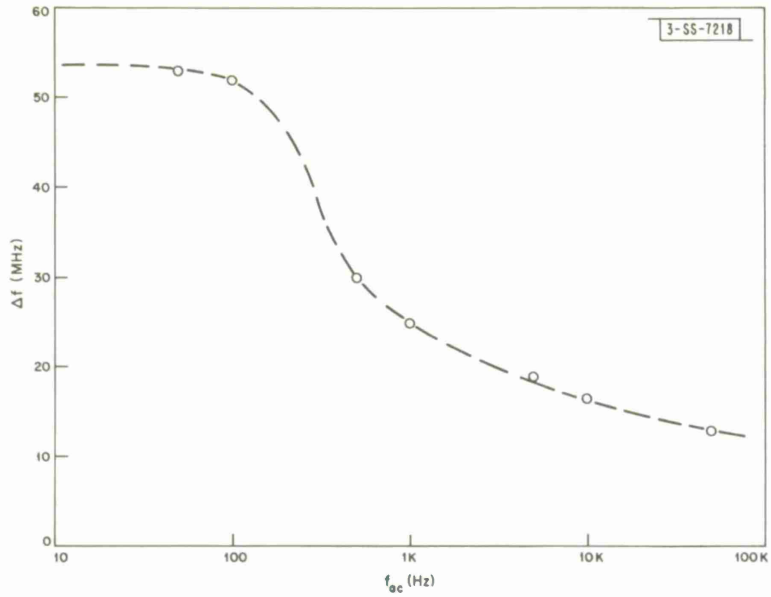

Fig. II-4. Frequency spread of beat note corresponding to diode "ripple" currents of various frequencies. "Ripple" current amplitude is constant at 4 mA peak to peak.

Since the index of refraction is a function of magnetic field as well as temperature, tuning the laser emission frequency may be accomplished at a faster speed by using the magnetic field from a small coil surrounding the diode laser. In an initial experiment to determine the influence of a bar magnet on the heterodyne beat frequency, an 8-G magnetic field produced a 30-MHz shift in the beat frequency – a rate comparable with that obtained previously from optical data.[7]

4. Quantum Phase Noise: Diode Laser Linewidth

Previous experiments[4] have indicated that the linewidth of a 200-μW $Pb_{0.88}Sn_{0.12}Te$ diode laser is less than 100 kHz; but more exact measurements were precluded because of modulation of the laser output frequency by ripple in the current supply. According to Schawlow and Townes[8] the ultimate spectral purity of any laser is determined by quantum phase noise which produces a Lorentzian-shaped frequency distribution profile with half-power width

$$\Delta\nu = (\pi h\nu/P)\,(\Delta\nu_c)^2 \quad , \tag{I-5}$$

where P is the mode power and $\Delta\nu_c$ the cold-cavity bandwidth. The emission from a low-power, battery-operated $Pb_{0.88}Sn_{0.12}Te$ diode laser was heterodyned with the P_{20} transition line from a CO_2 laser. A rough calculation from Eq. (I-5) indicates that the linewidth of the diode laser should be, because of its low power, of the order of a few megahertz. The spectrum analyzer displays of the beat note are shown in Figs. II-5(a-d), where each photograph depicts a 1-sec exposure. The vertical scale is proportional to detector current. Each picture represents a different diode laser power (related to the vertical amplitude) obtained by changing the diode current while maintaining a fixed beat frequency of 1180 MHz by external adjustment of the heat sink temperature. The modulation envelopes differ markedly from the relatively flat-topped shape produced by ripple in the diode current, and more nearly approximate the theoretical shape.

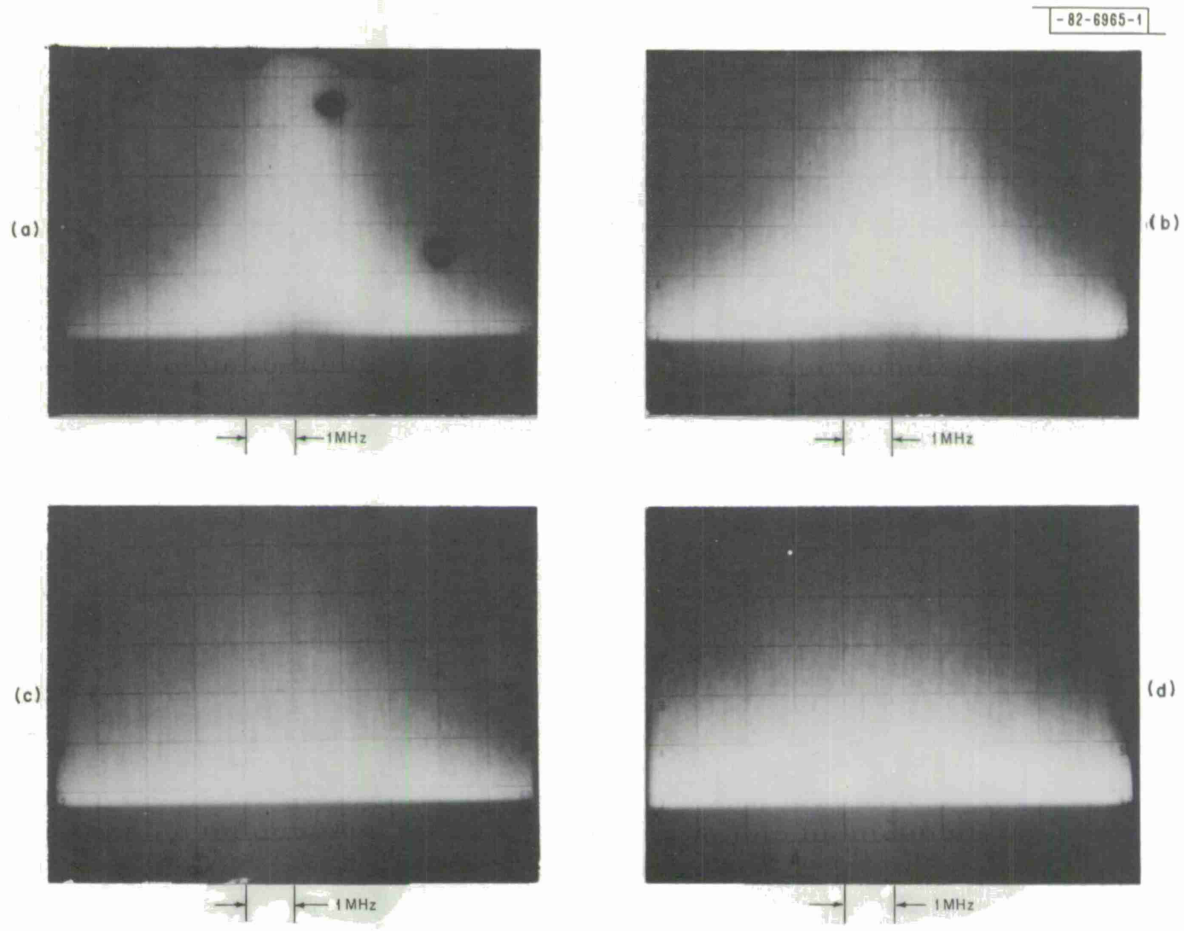

Fig. II-5. Power spectrum of 1180-MHz beat note for different diode laser power levels. Identical vertical scales are proportional to detector current. Each figure represents 1-sec exposure time with 3-msec/cm sweep rate.

Laser power diminishes from (a) to (d), with an apparent concomitant increase in linewidth, in qualitative agreement with Eq. (I-5). Carefully integrated power spectral density plots are required for quantitative verification of the Schawlow-Townes equation; such experiments are being planned.

Figure II-6 is a typical photograph illustrating the narrowest beat note obtained for stable laser operation to this point. The diode laser linewidth is approximately 100 kHz, but mechanical vibrations occurring during the 1-sec exposure create additional modulation of the beat note.

5. Infrared Detector Frequency Response Measurements

One of the main practical uses for tunable infrared laser heterodyning is to measure the frequency response of infrared detectors. Of particular interest is the Ge:Cu detector which is to be used in the CO_2 Doppler radar system, and which must respond to heterodyne frequencies of over 1 GHz. By a multiple-exposure photographic technique, in which the spectrum analyzer display was recorded at every 100-MHz beat frequency interval from zero to 2 GHz, the photograph of Fig. II-7 was obtained. The vertical scale is proportional to detector current. The

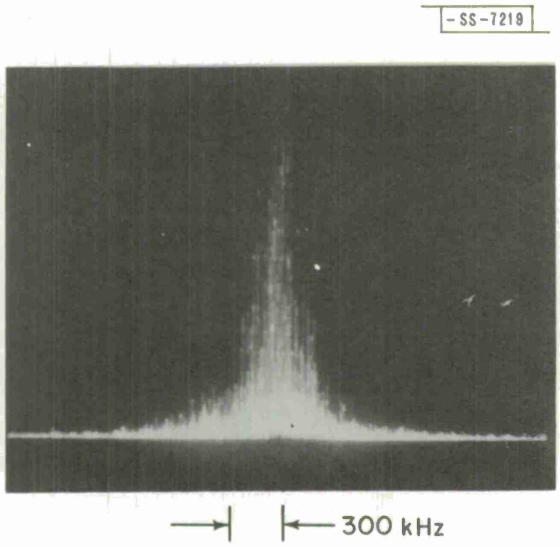

Fig. II-6. Square-law spectrum analyzer display of narrowest beat frequency spread observed to date for battery-powered diode laser. Exposure time is 0.25 sec, sweep rate 10 msec/cm.

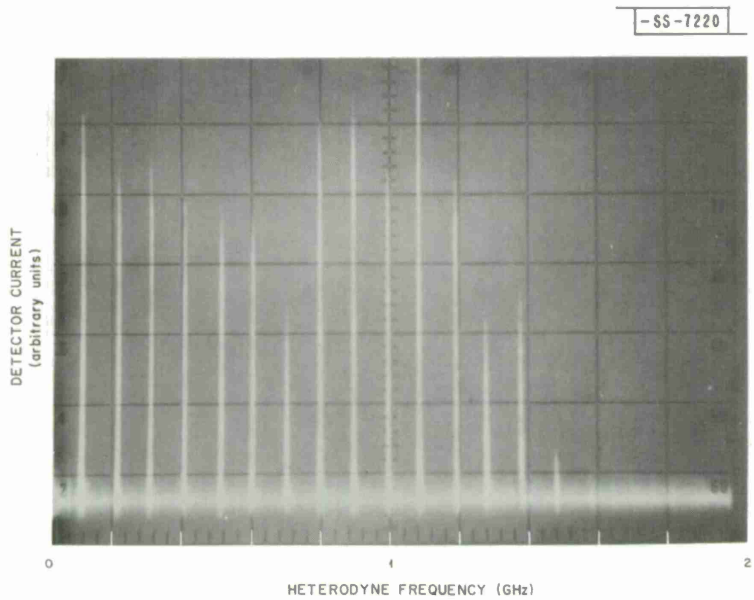

Fig. II-7. Frequency response of Ge:Cu detector at liquid helium temperature, uncorrected for variations in spectrum analyzer gain or diode laser power. Photograph represents 20 exposures corresponding to 100-MHz beat frequency intervals to 2 GHz. Carrier lifetime from blackbody responsivity data is 2×10^{-10} sec.

detector carrier lifetime, as determined by blackbody responsivity measurements, is 2×10^{-10} sec, which agrees with the indicated high-frequency cutoff of 1.4 GHz. By taking the measurements with the diode laser frequency both above and below the P_{20} line, it is possible to nullify any irregularities caused by variations in the diode laser output power with current; in particular, the large dip at 700 MHz was not observed when the measurements were repeated with the diode laser emission on the opposite side of the P_{20} line, so that the dip is not characteristic of either the detector or its circuitry. The general unevenness of the spectral lines for different beat frequencies may be caused partly by the spectrum analyzer itself, so that for more accurate measurements a reference signal must be used.

E. D. Hinkley
C. Freed
T. C. Harman

REFERENCES

1. Solid State Research Reports, Lincoln Laboratory, M.I.T. (1968:1), p. 11, DDC 668762, and (1968:2), DDC 672961, p. 13.
2. P. K. Cheo, J. Quantum Electron. QE-3, 683 (1967).
3. H. Kogelnik and T. J. Bridges, J. Quantum Electron. QE-3, 95 (1967).
4. Ref. 1 (1968:2), p. 16.
5. Alvin A. Machonis and Irving B. Cadoff, Trans. Met. Soc. AIME 230, 33 (1964).
6. W. E. Engeler and M. Garfinkel, J. Appl. Phys. 34, 2746 (1963).
7. J. F. Butler and A. R. Calawa, Physics of Quantum Electronics (McGraw-Hill, New York, 1966), p. 458.
8. A. L. Schawlow and C. H. Townes, Phys. Rev. 112, 1940 (1958).

III. MATERIALS RESEARCH

A. PREPARATION OF TELLURATE GARNETS $\{A_3\}[Te_2](B_3)O_{12}$

1. Garnets with Tetrahedral Co^{2+}

Recently Geller[1] has reviewed the compounds with garnet structure, listing the preferences of various cations for the dodecahedral {c}, octahedral [a], and tetrahedral (d) sites. He placed special emphasis on the strong preference of the Co^{2+} ion for octahedral sites. We have now prepared garnets containing Te in which the Co^{2+} ions occupy tetrahedral sites. It was anticipated that Te would occupy the octahedral sites in these compounds because octahedral $(TeO_6)^{6-}$ complexes are particularly stable. The garnets previously investigated either contain stable tetrahedral complexes or do not contain any stable complex.

The compounds $Ca_3Te_2Zn_3O_{12}$, $Ca_3Te_2ZnCo_2O_{12}$, $Cd_3Te_2Zn_3O_{12}$ and $Cd_3Te_2Zn_2CoO_{12}$ have been prepared by sintering stoichiometric mixtures of oxides and carbonates at temperatures between 900° and 1050°C. It was not possible to replace Zn entirely with Co in either the Ca or Cd compounds. From x-ray intensity data it has been possible to confirm the cation distribution of $\{Ca_3\}[Te_2](Zn_3)O_{12}$, with Te in the octahedral sites as expected. The color of $Ca_3Te_2ZnCo_2O_{12}$ is brilliant blue, showing that Co^{2+} occupies the tetrahedral sites. This is quite probably the case for $Cd_3Te_2Zn_2CoO_{12}$ also, although its blue-green color does not establish the tetrahedral site conclusively.

The Co^{2+} garnets discussed by Geller[1] contain dodecahedral A^{3+} cations. The octahedral site preference of Co^{2+} in these compounds can be attributed to the electrostatic repulsive force between A and B (tetrahedral) ions. When the A cation is triply charged, this force is too large to permit the relatively large Co^{2+} ion to occupy the B site. A smaller charge on the A cation reduces the electrostatic A-B interaction, and a smaller size A cation allows greater screening of the interaction via the intermediary anion.

2. Garnets of Type $\{Na_3\}[Te_3](B_3^{3+})O_{12}$

The preparation of tellurate garnets with $A_3^{2+}B_3^{2+}$ cation suggested the possibility of replacing these ions with either $A_3^{+}B_3^{3+}$ or $A_3^{3+}B_3^{+}$. Because of the importance of the A-B repulsive force, it is necessary that A and B be of proper size. In fact, the $Na_3^{+}B_3^{3+}$ garnets $Na_3Te_2Al_3O_{12}$ and $Na_3Te_2Ga_3O_{12}$ have been prepared, but $Na_3Te_2Fe_3O_{12}$ could not be.

3. Rare Earth Garnets $\{Ln_3\}[Te_2](Li_3)O_{12}$

The substitution $A_3^{3+}B_3^{+}$ has also proved successful, with the small Li^{+} ion as B^{+} and A = Pr, Nd, Sm, Eu, Gd, Tb, Dy, Ho, Er, Tm, Yb, or Lu. These compounds are formed by sintering around 800°C. The x-ray diffraction films show very sharp lines which indicate good crystallization, and it seems probable that single crystals can be grown. The Nd compound is insoluble in water but soluble in hydrochloric acid. According to x-ray diffraction data, the Pr compound was decomposed into pyrochlore-like compounds by sintering at 1300°C. Similar compounds

were obtained when an unsuccessful attempt was made to prepare the La garnet by sintering at 800°C.

H. M. Kasper

B. POLYMORPHISM IN $CdCr_2Se_4$ AT HIGH PRESSURE

$CdCr_2Se_4$ is one of a family of compounds of the general formula AB_2X_4, where A and B are divalent and trivalent metal atoms, respectively, and X is O, S, Se, or Te. These compounds crystallize with either the cubic spinel structure or a monoclinic distortion of the NiAs structure. In the former, the anions form an essentially cubic close-packed lattice with the A atoms in the tetrahedral holes and the B atoms in the octahedral holes. In the latter, the anions have hexagonal packing with the A and B atoms in the octahedral holes, and the vacancies are ordered to give an overall monoclinic structure. (If the vacancies were disordered, the structure would be the NiAs type, with hexagonal symmetry.) The oxides form only spinels, and the sulfides are found in either the cubic or monoclinic structures. The selenides and tellurides are found primarily in the monoclinic form, but $CdCr_2Se_4$ and $CuCr_2Se_4$ have the cubic structure because the A cations are strongly stabilized on the tetrahedral sites.

$CdCr_2Se_4$ is of current interest because it is a ferromagnetic semiconductor[2,3] with a nonmagnetic ion in the A sites. Small single crystals have been grown by various methods,[4,5] and their properties studied.[5,6] It has not been possible to grow crystals from the melt, since at atmospheric pressure $CdCr_2Se_4$ decomposes to CdSe and Cr_2Se_3 at ~700°C (Ref. 7). Recently we attempted to grow larger crystals by prolonged heating of the compound at 700° to 750°C under elevated pressures. It was found that at these temperatures, pressures over 20 kbars transform the spinel phase into a new phase with the monoclinic defect-NiAs structure, which can be retained at atmospheric pressure by quenching to room temperature before dropping the pressure.

We have employed several methods to prepare the spinel form of $CdCr_2Se_4$ for use as starting material in studying the high pressure phase. Two types of material have been obtained. The first was a loosely sintered ingot which was evaluated both by taking long exposure x-ray diffraction powder patterns and by hot-pressing in gold capsules at 10 kbars and 500°C to produce a dense compact for metallographic examination. Even samples which showed no CdSe or Cr_2Se_3 lines in the x-ray patterns frequently contained ~1 percent of CdSe (identified by electron microprobe analysis) visible in the compacts as isolated islands. Chemical analysis showed that ingots with no excess CdSe had the stoichiometric composition to within 1 percent (for example, $CdCr_{1.99}Se_{4.03}$). No results of metallographic examination or chemical analysis have previously been reported for $CdCr_2Se_4$.

The other type of reaction product, which was obtained by growth from a $CdCl_2$ melt, consisted of crystals varying in size from less than 0.1 to over 2 mm in diameter, as shown in Fig. III-1. The smaller crystals were generally well developed octahedra with some undeveloped faces, pits, and intergrowth of other crystals. Crystals with diameters greater than 1 mm were all intergrown clusters having large voids and pockets. Metallographic examination showed that single crystals 0.5 to 1 mm in diameter were free of inclusions. Larger crystals, even those selected to have the minimum of intergrowth and twinning, always contained CdSe and sometimes Cr_2Se_3 inclusions (identified by electron microprobe analysis), as shown in Fig. III-2.

-SS-7222

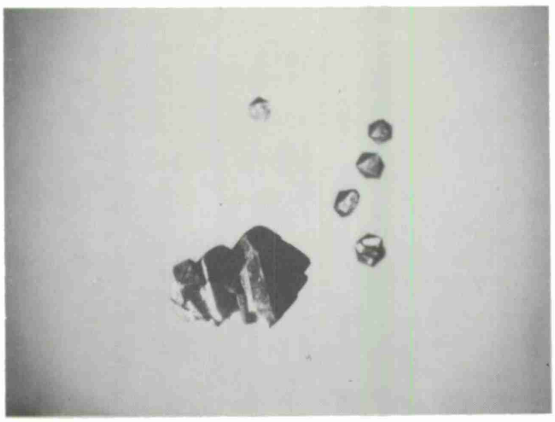

Fig. III-1 Crystals of $CdCr_2Se_4$ grown from $CdCl_2$ melt. Large crystal is about 2 mm long.

-SS-7223

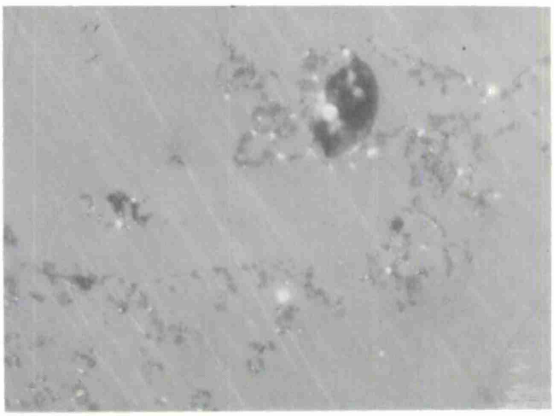

Fig. III-2. Polished surface of large $CdCr_2Se_4$ crystal, showing inclusions of Cr_2Se_3 (200X).

Chemical analysis of one batch of crystals showed that the small crystals (0.5- to 1-mm diameter) were stoichiometric ($Cd_{1.000}Cr_{1.998}Se_{4.041}$) while the larger ones (1- to 2-mm diameter) contained about 5 mole percent excess CdSe. The cubic lattice parameter for the stoichiometric crystals was found to be 10.746 ± 0.002 Å, compared with 10.755 Å (Ref. 3) and 10.721 Å (Ref. 6) given in the literature for samples with no reported analysis. It is possible that the spinel phase has an appreciable range of homogeneity and that the variation in the lattice parameters is due to differences in sample composition.

To prepare samples of the high pressure phase and to study the pressure-temperature phase diagram for $CdCr_2Se_4$, single-phase spinel samples were sealed in gold capsules and annealed at pressures from 10 to 50 kbars and temperatures from 350° to 800°C for 20 hours to 3 days. A 1-inch piston-cylinder high pressure unit was used for pressures to 25 kbars, and a 2000-ton per ram tetrahedral-hinge unit was used for the higher pressures. Temperature control was generally better than ±10°C over 24 hours. At the end of each run, the temperature was dropped rapidly to quench-in the phase formed under the annealing conditions, while the pressure was generally dropped slowly to minimize cracking of the sample. The gold was then peeled off and the sample was examined metallographically and by x-ray diffraction. Electrical and magnetic measurements were made on some samples, and some were analyzed chemically.

Whereas the spinel form of $CdCr_2Se_4$ is a semiconductor, the high pressure phase shows metallic conduction, with a resistivity of 2 to 5×10^{-2} ohm-cm at room temperature and a small positive temperature coefficient of resistivity. The high pressure phase has no superconducting transition down to 1.35°K. Its magnetic moment is only $\sim 0.035\mu_B$, compared with $5.6\mu_B$ for the spinel phase. According to a preliminary indexing of the x-ray diffraction patterns, it has the monoclinic defect-NiAs structure, which has also been reported for the high pressure phase of $FeCr_2S_4$ (Ref. 8). Thus high pressure appears to force the Cd atoms into octahedral coordination and transforms $CdCr_2Se_4$ into the same structure as the other compounds of the AB_2Se_4 series. The increase in coordination for Cd is expected for atoms with low coordination when subjected to high pressures. Likewise, the transition from semiconducting to metallic electrical behavior is expected from this treatment. The measured density of a sample of the high pressure phase

is 5.77 g/cm^3. This represents an increase of ~3 percent over the measured density of a hot-pressed sample of the spinel phase, 5.59 g/cm^3.

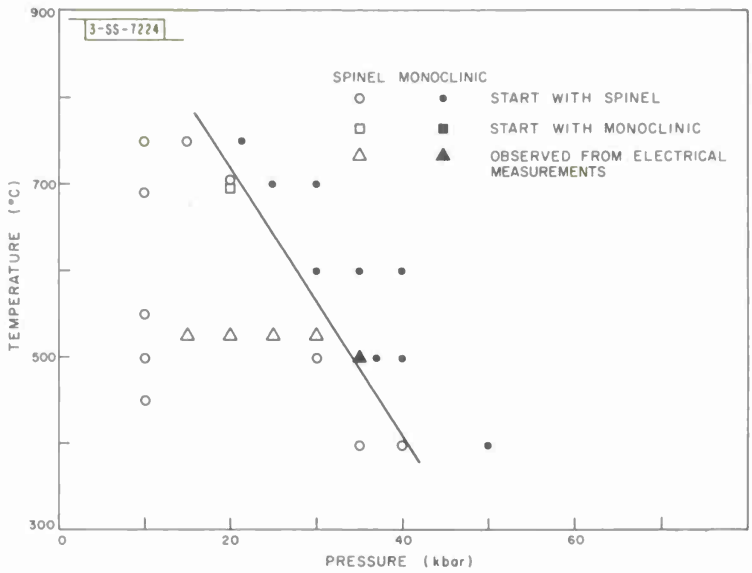

Fig. III-3. Pressure-temperature diagram for $CdCr_2Se_4$.

The phase diagram obtained from the annealing experiments is shown in Fig. III-3. The phase boundary between the spinel and monoclinic phases has a negative slope. Extrapolation of the boundary indicates that at one atmosphere the spinel phase would transform to the monoclinic phase at about 1000°C. This cannot be observed because of the decomposition of $CdCr_2Se_4$ above 700°C at this pressure. At 10 kbars, decomposition occurs at 800°C. At room temperature, the transformation should take place at ~70 kbars, but it may be too slow to detect. In one experiment, the retransformation from monoclinic to spinel was observed after 24 hours at 20 kbars and 700°C.

A series of runs at various fixed pressures was made to follow the electrical resistivity of $CdCr_2Se_4$ as a function of temperature. At 15, 20, and 25 kbars, the resistivity decreased smoothly, approximately 3 orders of magnitude between 25° and 525°C, and returned to the initial value on cooling to room temperature. At 30 kbars, the resistivity was appreciably lower on returning to room temperature. After repeating the cycle with a 9-hour hold at 525°C, the room temperature resistivity was one-tenth the initial value at this pressure, indicating partial transformation. At 35 kbars, the resistivity decreased steadily on cooling from 500°C, showing metallic conduction characteristic of the high pressure phase.

It appears that the x-ray diffraction patterns of samples pressed at 25 and 30 kbars and 700°C may be better indexed on a hexagonal cell rather than a monoclinic cell. The hexagonal NiAs structure is obtained if the cation vacancies are randomly oriented. It has also been reported that $FeCr_2S_4$ pressed at 35 to 40 kbars and 1100°C has the NiAs structure,[9] while the same compound pressed at 65 kbars and 1000°C has the monoclinic defect-NiAs structure.[8] Partial transformation of $CuCr_2Se_4$ from spinel ["spinel" is a specific structure, whereas "hexagonal" is a class] to a hexagonal structure at high pressures has also been observed.[8] Thus $CdCr_2Se_4$ and

$CuCr_2Se_4$, the two compounds of the AB_2Se_4 family which do not have all the metal atoms in octahedral symmetry at atmospheric pressure, are both forced into this symmetry by treatment at high pressure.

M. D. Banus A. Ferretti
M. C. Lavine T. E. Stack

C. HIGH PRESSURE FORM OF $CsNiF_3$ – A TRANSPARENT FERRIMAGNET

The atmospheric pressure form of $CsNiF_3$ (hexagonal, a = 6.236 Å, c = 5.225 Å) consists of hexagonal close-packed layers of CsF_3 with Ni^{2+} occupying the fluorine octahedra. These octahedra are face-shared to form infinite chains along the c-axis.[10] The structure type, which contains two layers in the unit cell, has been designated as (2L), and its relationship to other close-packed ABX_3 structures has been discussed elsewhere.[11]

A high pressure form of $CsNiF_3$ has been prepared by reacting equimolar mixtures of CsF and NiF_2 at 700°C and 65 kbars for 1/2 hour. The dry reactants are weighed, thoroughly ground together, and loaded into a gold capsule in a glove bag filled with dry nitrogen. If these precautions are not taken, impurity phases appear in the product.

X-ray diffraction measurements using a Norelco vertical goniometer with CuKα radiation gave a pattern for powdered samples of the high pressure phase which has been indexed using a hexagonal cell with a = 6.05 Å, c = 14.54 Å. The intensities of the diffraction peaks are consistent with a structure isomorphous with that of the atmospheric pressure form of $RbNiF_3$ (Fig. III-4). This structure contains cubic (c) and hexagonal (h) close-packed RbF_3 layers in the sequence (cchcch) and is designated (6L) (Ref. 11). The NiF_6 octahedra share both corners and faces such that there are face-shared pairs connected by an octahedron which shares only corners to give a three-dimensional network.

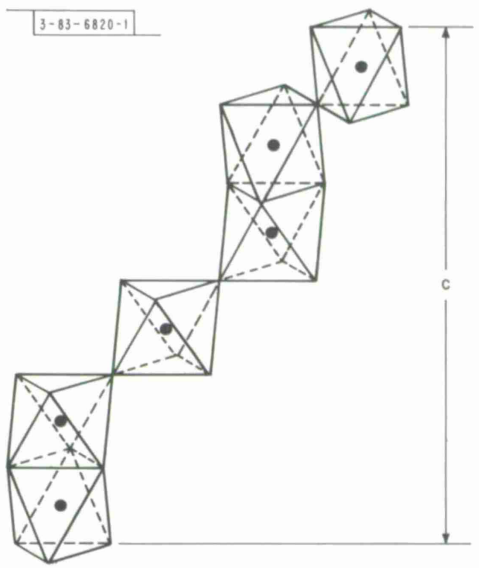

Fig. III-4. Schematic of [110] plane of hexagonal cell for $RbNiF_3$ (6L), showing face and corner sharing by octahedra between RbF_3 layers.

Once formed at elevated pressures, $CsNiF_3$ (6L) is retained at atmospheric pressure at temperatures up to several hundred degrees Celsius. There is a 10-percent reduction in volume in the transformation from the (2L) form (85.4 $Å^3$/molecule) to the high pressure (6L) form (76.8 $Å^3$/molecule).

Magnetic susceptibility measurements on the light yellow, transparent $CsNiF_3$ (6L) give a ferrimagnetic T_c = 111°K. The change in T_c with pressure $\Delta T_c/\Delta p$ = +0.53 deg/kbar. For $RbNiF_3$ (6L), which is also a light yellow, transparent ferrimagnet, T_c = 139°K and $\Delta T_c/\Delta P$ = +0.60 deg/kbar.

J. Longo D. Batson
J. Kafalas T. Hilton

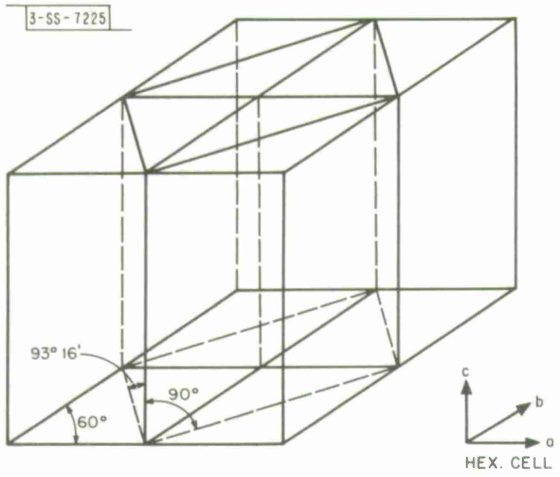

Fig. III-5. Relationship between monoclinic unit cell of atmospheric pressure form of $SrIrO_3$ and hexagonal unit cell of $RbNiF_3$ (6L).

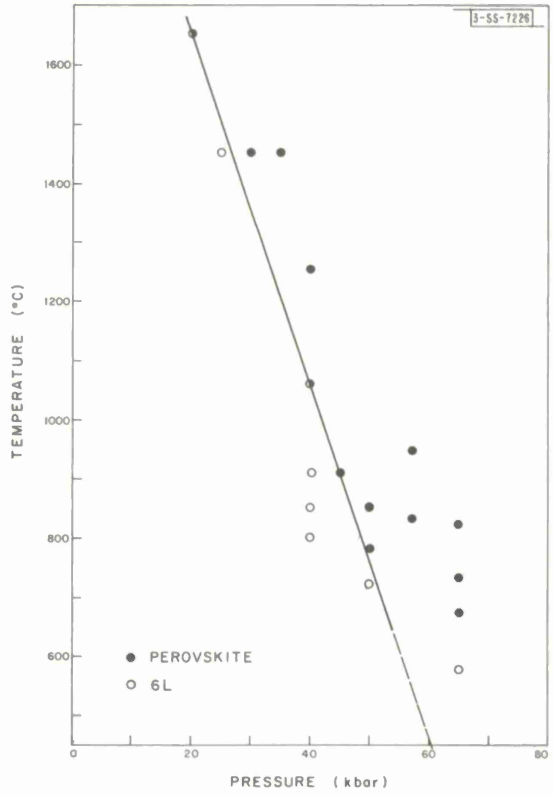

Fig. III-6. Pressure-temperature diagram for $SrIrO_3$.

D. LOW AND HIGH PRESSURE FORMS OF $SrIrO_3$

Preparation of $SrIrO_3$ at atmospheric pressure has been reported,[12] but no structural information has been available. We have indexed the x-ray powder pattern for this compound by using a monoclinic unit cell with parameters a = 5.60 Å, b = 9.62 Å, c = 14.17 Å, and β = 93.26°. The atomic arrangement is closely related to that of the hexagonal (6L) form of $RbNiF_3$ (see Sec. III-C). The relationship between the monoclinic (m) and hexagonal (h) unit cells is given by the following expressions: $a_m \approx a_h$, $b_m \approx \sqrt{3}\, b_h$, and $c_m \approx c_h$. This relationship is also illustrated by Fig. III-5. $SrIrO_3$ is the first compound for which the hexagonal (6L) structure has been found to be distorted.

At high pressures and elevated temperatures, the atmospheric pressure phase of $SrIrO_3$ is transformed into an orthorhombically distorted perovskite phase with the following lattice parameters: a = 5.58 Å, b = 5.60 Å, c = 7.89 Å. The pressure-temperature diagram for $SrIrO_3$ up to 65 kbars and 1700°C is given in Fig. III-6, which shows the phase boundary between the low and high pressure forms determined by means of annealing experiments. There is a 3-percent reduction in volume when the low pressure (6L) form (63.5 $Å^3$/molecule) is transformed into the perovskite form (61.6 $Å^3$/molecule).

Magnetic susceptibility measurements to 4.2°K and 17 kOe show that the perovskite form exhibits temperature-independent Pauli paramagnetism. This behavior is consistent with the very high electrical conductivity of this phase.

It is interesting to note that Ir^{4+} is one of the few ions which form $SrM^{4+}O_3$ compounds with the hexagonal (6L) structure. For M = Ti, Zr, Hf, Mo, Tc, Ru, Sn, and Pb, the perovskite structure is obtained. Low spin Ir^{4+} would have five electrons in the t_{2g} orbitals, with one of them unpaired. This gives Ir a very strong tendency to form metal-metal bonds and therefore favors the (6L) structure, since the face-shared octahedra of this structure allow the Ir atoms to approach close enough to form such bonds.

J. M. Longo D. A. Batson
J. A. Kafalas T. W. Hilton

E. CRYSTALLOGRAPHIC AND MAGNETIC PROPERTIES OF PEROVSKITE AND PEROVSKITE-RELATED COMPOUNDS

An extensive summary of the crystallographic and magnetic properties of perovskite and perovskite-related compounds, with an interpretive introduction and over 1500 references, has been prepared for the Landolt-Bornstein Tabellen. The Table of Contents follows:

I. Introduction
  - A. General Remarks
  - B. Symbols and Units Used in Tables and Figures

II. Descriptions of Stoichiometric ABX_3 and $M^cXM_3^f$ Structures
  - A. The Ideal Perovskite Structure
  - B. The Influence of Relative Ionic Sizes
    1. Tolerance Factor
    2. O-orthorhombic Structure
    3. Rhombohedral Structures

C. The Influence of Localized-Electron Ordering
   1. Crystal-Field Theory
   2. Jahn-Teller Distortions
   3. Spin-Orbit Coupling

D. The Influence of Collective-Electron Ordering
   1. Band Theory
   2. Distortions Due to B-X Bonding
   3. Distortions Due to Core Polarization: Pb^{2+} and Bi^{3+}
   4. Competitive Phases

E. Structures Encountered with Ordered B, B' Cations
   1. Same B Atom
   2. Different B Atoms
   3. Complex Alloys $A_2BB'X_6$, where $B = M_{13}$, $B' = M'_8$

F. First-Order Magnetic Transitions in $M^cXM_3^f$ Perovskites

III. Descriptions of Perovskite-Related Structures

A. A-Cation Vacancies
   1. No A-Cation
   2. The Bronze Structures

B. Anion-Deficient Compounds
   1. Compounds ABX_{3-x}
   2. Alloys $M^cX_{1-x}M_3^f$.
   3. Shear Structures $\square BO_{3-x}$

C. Structures Deficient in B Cations
   1. Bismuth Compounds
   2. Hexagonal $A_nB_{n-1}X_{3n}$ Structures
   3. $AX \cdot (ABX_3)_n$ Structures

IV. Magnetic Order: Localized Electrons

A. Phenomenological Exchange Hamiltonian

B. Microscopic Models
   1. Isotropic Superexchange
   2. Double Exchange
   3. Anisotropic Superexchange

C. Parasitic Ferromagnetism
   1. Definition
   2. Anisotropy Considerations
   3. Antisymmetric Superexchange

V. Localized Vs Collective Electrons

A. Introduction

B. Integral n_d
   1. Construction of an Electronic Phase Diagram
   2. Distinguishing Physical Properties Imparted by Different Electronic Phases

C. Nonintegral $n_d = 1 \pm c$

D. Energy Diagrams for ABX_3 Perovskites

VI. The $M^cXM_3^f$ Alloys

J. B. Goodenough
J. M. Longo

F. LOW-LYING ENERGY LEVELS AND LASER ACTION OF U^{+3} IN CaF_2:$NaUF_4$

Intense fluorescence from CaF_2:U^{+3} in the 2.5-μ spectral region was first observed by Galkin and Feofilov.[13] On the basis of this work, Sorokin and Stevenson[14] produced the first four-level laser. Pulsed laser action from U^{+3}-doped BaF_2 has been reported by Bostick and O'Connor.[15] These papers do not contain any additional spectroscopic studies of U^{+3} in CaF_2.

The method by which U^{+3} is charge-compensated in a CaF_2 crystal can affect both the energy level system and laser efficiency. This has prompted us to investigate the properties of U^{+3} compensated by Na^{+1} ions located at nearest substitutional cation sites. The advantages of this method of charge compensation are that substantially all the U^{+3} ions will have orthorhombic symmetry and that no U^{+2} or U^{+4} ions are likely to be formed.

Infrared absorption was measured at 77° and 4.2°K by using a NaCl fore prism and a Perkin-Elmer (99-G) grating spectrometer. The grating had 600 lines/mm and was blazed at 2.5 μ. The absorption spectrum of CaF_2:$NaUF_4$ at 77°K is shown in Fig. III-7. Line positions are accurate to ~5 Å but line widths are slit-limited to ~2 cm^{-1}. Six sharp lines are observed from 2.202 to 2.256 μ. These are identified as transitions from the $^4I_{9/2}$ ground state to Stark split levels of the $^4I_{11/2}$ multiplet. Four vibronic levels are identified. These occur at 42 ± 2 cm^{-1} on the

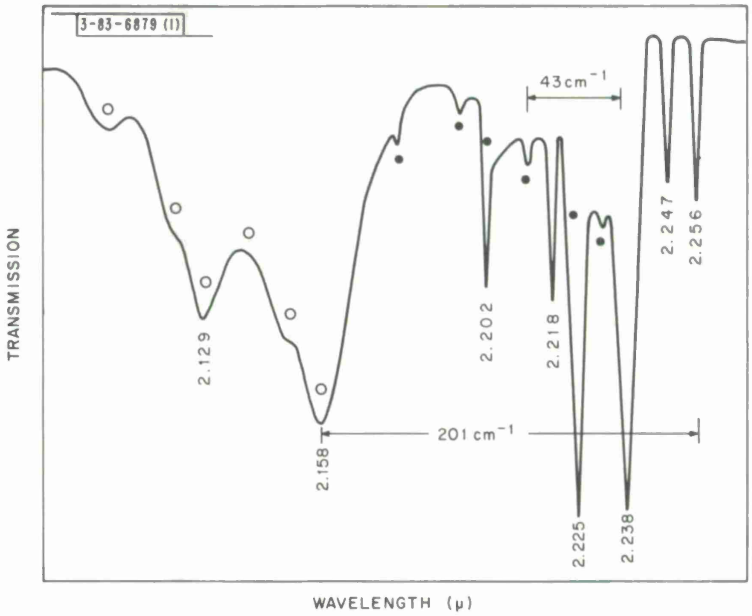

Fig. III-7. Relative absorption spectrum at 77°K of CaF_2 doped with 0.1% $NaUF_4$. Closed circles indicate the positions of 6 vibronic levels. Open circles indicate 6 infrared Raman vibrations.

TABLE III-1

THRESHOLD FOR LASER ACTION AT 77°K IN $CaF_2:U^{+3}$

Compensator	Site Symmetry (percent)	Emission Wavelength (μ)	Terminal Level (cm^{-1})	Threshold (joules)
O^{-2}	90 trigonal	2.225	0	150
F^{-1}	90 tetragonal	2.436	389	16
F^{-1}	90 tetragonal	2.513	471	7
F^{-1}	90 tetragonal	2.563	607	5
F^{-1}	90 tetragonal	2.613	607	4
F^{-1}	50 tetragonal, 30 orthorhombic	2.613	607	2
Na^{+1}	90 orthorhombic	2.613	607	<1

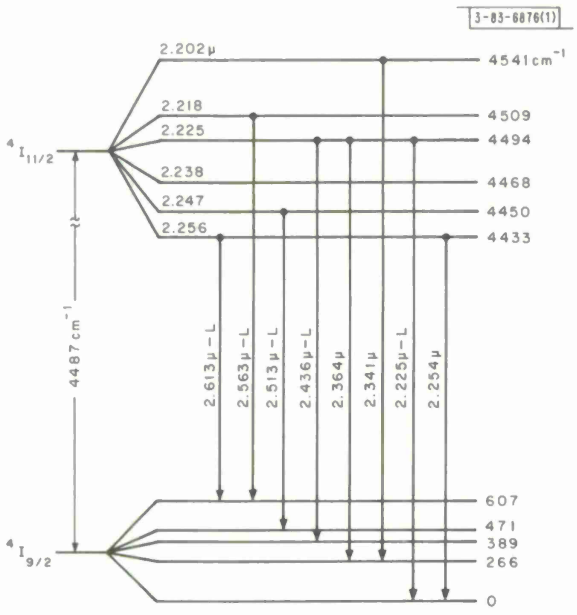

Fig. III-8. Energy level diagram for U^{+3} in CaF_2. Laser transitions are indicated by L.

energy side of each ground state transition. The reststrahlen frequency of CaF_2 is 270 cm^{-1}. The reduced mass of a U^{+3} complex is greater than that in pure CaF_2 by a factor of six. The coupling or vibrational energy should therefore be ~45 cm^{-1}. Vibronic energy levels have been previously observed in $Ca_2UO_2Cl_4$ at an energy of 46 cm^{-1} by Conn and Wu.[16] At a higher energy, ~200 cm^{-1} from ground state transitions, six broad absorptions are observed. We assign these strong absorptions to infrared-active, Raman processes that are frequently observed in U compounds at 210 cm^{-1}. This energy (210 cm^{-1}) is commonly assigned to the low frequency, breathing modes of U-O, U-Cl, etc. complexes.

The pulse laser thresholds at 77°K of a number of $CaF_2:U^{+3}$ crystals were determined using conventional apparatus.[17] The results are given in Table III-1. The transitions associated with laser emission are indicated on the energy level diagram shown in Fig. III-8. The correlation between the position of the terminal energy level and the threshold for laser action is obvious. It should be possible to improve the optical quality of Na^{+1} compensated crystals; lower thresholds should then result.

J. R. Connor

G. CHEMICAL ANALYSIS OF Zn-Te-Se ALLOYS

A method has been developed for the analysis of Zn-Te-Se alloys which is accurate to within a few parts per thousand for each component. The sample is dissolved in dilute aqua regia. The Se and Te are determined by classical oxidation-reduction methods using automatic titration equipment. The sum of Te and Se is determined by oxidation with potassium permanganate, while Te only is determined on a separate aliquot by oxidation with potassium dichromate; in both cases, excess oxidant is used and back titrated to a potentiometric end point with ferrous ammonium sulfate.

The Zn concentration is determined on another portion of the sample solution by an x-ray fluorescence method. Appropriate standard solutions are made from stock solutions of pure Zn, Te and Se metals, care being taken that the standards have the same acid content as the samples. The Zn$K\alpha$ line is excited by a W tube operated at 25 kV and 25 mA, dispersed with a LiF crystal and detected with a scintillation counter using a pulse height analyzer.

I. Searles
E. B. Owens

REFERENCES

1. S. Geller, Z. Krist. 125, 1 (1967).
2. N. Menyuk, K. Dwight, R.J. Arnott and A. Wold, J. Appl. Phys. 37, 1387 (1966), DDC 642203.
3. P.K. Baltzer, W.H. Lehmann and M. Robbins, Phys. Rev. Letters 15, 493 (1965).
4. H. von Phillipsborn, J. Appl. Phys. 38, 955 (1967).
5. S.B. Berger and H.L. Pinch, J. Appl. Phys. 38, 949 (1967).
6. R.C. LeCraw, H. von Phillipsborn, and M.D. Sturge, J. Appl. Phys. 38, 965 (1967).
7. H. Hahn and K.F. Schroder, Z. Anorg. Allgem. Chem. 269, 135 (1952).
8. R.J. Bouchard, Mat. Res. Bull. 2, 459 (1967).
9. W. Albers and C.J.M. Rooymans, Solid State Comm. 3, 417 (1965).
10. D. Babel, Z. Naturforsch. 20a, 165 (1965).
11. Solid State Research Report, Lincoln Laboratory, M.I.T. (1968:2), p. 28, DDC 672961.
12. F. Rodi, Thesis, Eberhard-Karls University, Tubingen (1963).
13. L.N. Galkin and P.P. Feofilov, Doklady AN 114, 745 (1957); Optics Spectrosc. 1, 492 (1959).
14. P.P. Sorokin and M.J. Stevenson, Phys. Rev. Letters 5, 557 (1963).
15. H.A. Bostick and J.R. O'Connor, Proc. IRE 50, 219 (1962).
16. G.K.T. Conn and C.K. Wu, Trans. Faraday Soc. 34, 1483 (1938).
17. J.R. O'Connor and W.H. Hargreaves, Appl. Phys. Letters 4, 208 (1964).

IV. PHYSICS OF SOLIDS

A. ELECTRONIC BAND STRUCTURE

1. Band Structure and Electrical Conductivity of NiO

It becomes apparent upon examining the recent optical and transport data for NiO that the localized crystal-field spectrum and the band-like, nonactivated mobility are incompatible properties if only d-electrons are considered. Aside from the fact that a d-band would be only partly filled, even taking into account exchange splittings, the multiplet excited states, which appear as discrete lines over a 4-eV energy range, would be condensed into the band continuum if the one-electron-band model were an appropriate description of the d-electron states. Although intricate polaron models have been constructed to reconcile these data, we find that the available data are consistent with a simpler model in which the conduction takes place in the one-electron-band states of the oxygen 2p band, while the d-electrons are described by the essentially localized many-electron states which give the multiplet structure. This description is illustrated in Fig. IV-1. The conductivity and absorption edge data indicate that the 2p-4s bands are separated by about a 4-eV energy gap, whereas the impurities provide acceptor centers 0.4 eV above the 2p valence band, as illustrated on the left side of the figure. On the right side, we schematically represent the ground state configuration of the 8 3d Ni^{2+} electrons, $3d^8$, and the excited many-electron states, $3d^{8*}$. The left and right sides of the diagram are not easily related to the same energy scale, since one side refers to many-electron states while the other side refers to one-electron states. To relate the two sides so that it is possible to represent transitions from, for example, the $3d^8$ ground state to the 4s conduction band by a single energy difference between two states, we have represented the true many-body states by equivalent pseudoparticle states which have the correct energy differences. This procedure allows us to portray all the known optical and transport data on a single diagram, analogous to the band structure diagram of simpler materials. This band structure is described more completely in an article which has been submitted for publication.

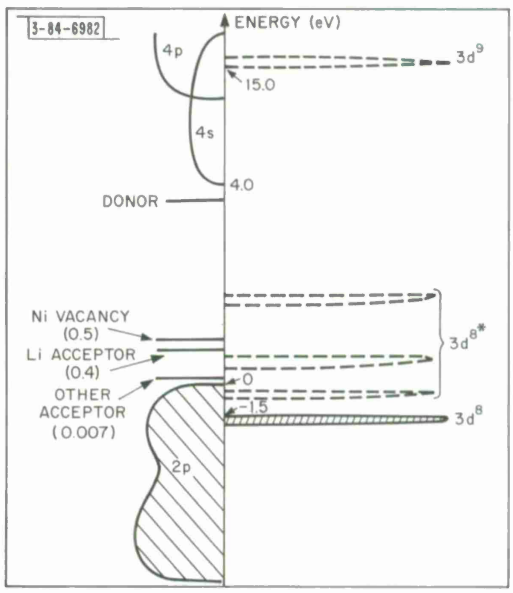

Fig. IV-1. Sketch of suggested density of pseudoparticle states for NiO. Conducting states are shown to left of vertical line, nonconducting states to right.

J. Feinleib
D. Adler†

† Department of Electrical Engineering, M.I.T.

2. Magneto-Optical Investigation of Bi-Sb Alloys†

Investigation of the band structure of Bi-Sb alloys‡ by oscillatory magnetoreflection has continued. As previously discussed,[1] this alloy system of these semimetals is of considerable interest because Hall and resistivity measurements indicate[2] semiconducting behavior at low temperatures in the range of composition $5 \lesssim \%\ \mathrm{Sb} \lesssim 40$. We have studied Bi-Sb alloys of 0, 3, 8, 12 and 15-percent antimony. To simplify the interpretation, the crystals were cut so that the light propagation and magnetic field were perpendicular to a binary face; for this configuration only one set of oscillations is observed. Figure IV-2 compares the magnetoreflection, at

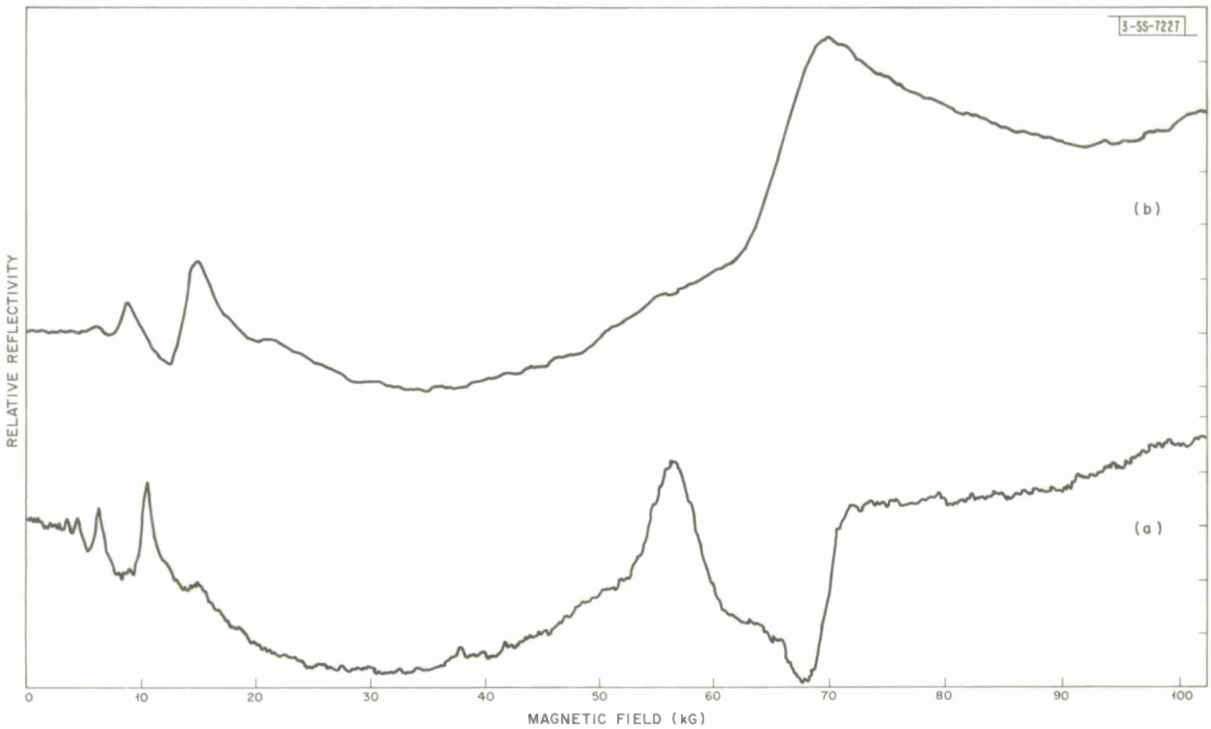

Fig. IV-2. Comparison between (a) pure bismuth and (b) 12-percent antimony alloy of oscillatory magnetoreflection from a binary face at $\hbar\omega = 0.07466$ eV and liquid helium temperatures.

a photon energy $\hbar\omega = 0.07466$ eV, of pure bismuth and a 12-percent antimony alloy. In pure bismuth at this photon energy, interband oscillations and also a sharp edge, at high magnetic fields, due to plasma-shifted cyclotron resonance are observed. The 12 percent antimony alloy at this same energy exhibits a number of differences. First, there is a shift in magnetic field of the interband oscillations indicating a change in the energy band parameters. Second there is a broadening of the lines because of increased alloy scattering. Third, the sharp plasma edge is gone and now cyclotron resonance is not shifted to lower fields but appears close to 100 kG, with a different line shape than in pure bismuth. This behavior is what one would expect from

† This experiment was carried out using the high field facilities of the Francis Bitter National Magnet Laboratory, M.I.T.
‡ We are indebted to Dr. W. M. Yim of RCA Laboratories for supplying these samples.

a semiconductor. The data, in combination with oscillatory transport measurements,[3] are now being analyzed in terms of the Lax two-band model. Preliminary results indicate an increase of energy gap and effective mass with increasing antimony concentration.

E. J. Tichovolsky†
J. G. Mavroides
D. F. Kolesar

B. TRANSPORT PHENOMENA

1. Transport Equation for Neutral or Charged Fermi Liquid in Random Impurities – Quasi-Particle Description for Weak and Slowly Varying Disturbances

The transport properties of an interacting Fermi gas in the presence of random impurities are studied by the generalization of a method developed by Resibois[4] for a pure interacting Fermi gas. A formula for the impurity averaged bare-particle distribution function is derived. A diagram technique is developed, and important lemmas involving the diagrams are proved, some of which depend essentially on the presence of the fermion-impurity interaction. An analysis of the diagrams leads to a transport equation for the bare-particle distribution function. Simplifications of this equation are considered for the case of slowly varying driving fields, low impurity density and low temperature.

The long range nature of the Coulomb interaction has been considered in the context of this formalism. The improper diagrams are shown to be taken into account by replacing the external field by the total average field. The calculation of the coefficients of the transport equation is made by the evaluation of the proper diagrams alone.

The formalism described above is used to calculate the coefficients of the transport equation to second order in both the interparticle and impurity interactions. It is shown that in terms of an appropriately defined quasi-particle distribution function, the transport equation is essentially the Landau quasi-particle transport equation with an appropriately defined impurity scattering term and an interparticle scattering term added. Since the equation is derived for the bare-particle distribution function, knowledge of the transformation between bare- and quasi-particle distribution functions is obtained.

A publication based on this work is in preparation.

J. L. Sigel
P. N. Argyres

2. Transport Equation for Dynamically Independent Fermions in Presence of Dilute But Arbitrarily Strong Impurity Scattering Centers

Using the techniques described in Sec. IV-B-1, we have calculated the coefficients of the transport equation to first order in the density of impurities and to all orders in the strength of the potential of a single impurity. In this work, we have made no restrictions on the frequency or wavelength of the external field.

† Department of Physics, M.I.T.

These results represent a generalization of the results of Luttinger and Kohn[5] who restricted themselves to the study of the response to a static, uniform disturbance.

Details of this work will be found in a forthcoming publication.

J. L. Sigel
P. N. Argyres

3. Transport Equation for a Fermi Liquid in the Generalized Random Phase Approximation in the Presence of Dilute, but Arbitrarily Strong Impurity Scattering Centers

Further applying the techniques mentioned in the above reports, we have included in the calculation of coefficients of the transport equation, terms of first order in the interparticle interaction. This amounts to a generalized random phase approximation.

Some of the effects found in this calculation are (a) renormalization of energy; (b) screening of the impurity potential by the fermions; and (3) screening of the external field in the Coulomb case.

Details of this work will be found in a forthcoming publication.

J. L. Sigel
P. N. Argyres

C. MAGNETISM

1. Effects of Pressure on Magnetic Properties of MnAs

At atmospheric pressure, MnAs undergoes a first-order hexagonal-orthorhombic transition at $T_1 \approx 315°K$. On further increasing the temperature, there is a continuous decrease of the orthorhombic distortion until it becomes zero at $T_2 \approx 400°K$, above which temperature the material is again in the hexagonal ($B8_1$) phase.[6] We have extended our study of the effect of pressure on the magnetic properties of MnAs to include a study of its paramagnetic susceptibility in the high temperature $B8_1$ phase.

Because of the loss in strength of the copper-beryllium bomb at higher temperatures, measurement in the high-temperature hexagonal phase was limited to the temperature interval between T_2 and 500°K, over which region the susceptibility behaves in accordance with the Curie-Weiss law. At atmospheric pressure, this permits measurement over a one-hundred-degree interval. However, over the pressure interval from one atmosphere to 3 kbars, T_2 was found to increase rapidly with pressure, in accord with the linear relationship $dT_2/dP = 23°K/kbar$. At higher pressures this reduced the temperature interval over which measurements could be made, and therefore reduced the accuracy of the extrapolation-determined paramagnetic Curie point $\Theta(B8_1)$.

Measurements of inverse susceptibility vs temperature at pressures of 1 atm and at 0.75, 1.5 and 2.25 kbars are summarized in Fig. IV-3. The resultant curves at all four pressures are consistent with a constant slope corresponding to $\mu_{eff}(B8_1) = 4.45\mu_B$ and to a pressure dependence $d\Theta(B8_1)/dP = -12°K/kbar$. These results at atmospheric pressure are in good agreement with those of Guillaud.[7] However, they are in marked contrast with the paramagnetic behavior of this sample in the orthorhombic (B31) phase, where we have found $\mu_{eff}(B31) = 2\mu_B$ and $d\Theta(B31)/dP = +7°K/kbar$.[8]

Bean and Rodbell[9,10] (B-R), have considered MnAs the outstanding example of a material with a first-order transformation caused by the presence of a strongly strain-sensitive magnetic

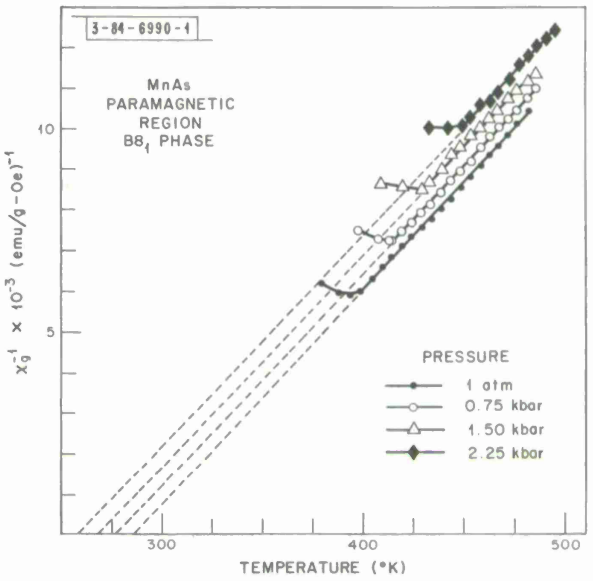

Fig. IV-3. Paramagnetic susceptibility curves of MnAs in high temperature hexagonal phase.

exchange interaction. The model used in their calculation assumed a single magnetic exchange interaction and isotropic elastic properties, and led directly to the equation

$$\frac{d\Theta}{dP} = -\Theta_o K\beta \qquad \text{(IV-1)}$$

where $d\Theta/dP$ is the pressure dependence of the Curie temperature, Θ_o is the value that the Curie temperature would have were the material incompressible, K is the compressibility $[-(1/V)(\partial V/\partial P)]$ and β is a measure of the strain sensitivity of the magnetic exchange. Since Θ_o is a large positive quantity in both the B31 and $B8_1$ phases (~200° to 300°K) and the compressibility K is of necessity a positive quantity, our direct measurements of $d\Theta/dP$ in both phase given above establish that, as defined by Eq. (IV-1), $\beta < 0$ in the orthorhombic phase and $\beta > 0$ in the hexagonal phase. However, this directly contradicts a fundamental assumption of the B-R model, namely, that β is a constant.

Although the B-R model in its present form is therefore inapplicable to MnAs, it of interest to establish whether a generalized model involving constant strain-sensitive exchange effects can account for the change in sign $d\Theta/dP$ and be consistent with the other known properties of MnAs. We found that removal of the restrictive (and unrealistic) assumptions of a single magnetic interaction and elastic isotropy could not account for the change of $d\Theta/dP$ if consideration of elastic energy was restricted to second order in the strains. However, extension of elastic energy considerations to third-order strain effects led to the equation

$$\frac{d\Theta}{dP} = \frac{2S(S+1)}{3k} \sum_v z_{uv} J^o_{uv} \left[\beta'^1_{uv} \frac{d\eta_1}{dP} - \sum_{i=2}^{3} \beta'^i_{uv} \frac{a_i}{\lambda_i} - \frac{L_{111}}{\lambda_i} \eta_1 \frac{d\eta_1}{dP} \right] \qquad \text{(IV-2)}$$

where k is Boltzmann's constant, S is the spin quantum number, z_{uv} is the number of v neighbors of a u atom, J^o_{uv} is the uv exchange interaction in the unstrained sample, β'_{uv} represents the sensitivity of this interaction to strain along the i^{th} coordinate axis (i = 1, 2, 3), the a_i correspond to transformation coefficients, the λ_i and L_{ijk} are the coefficients of the second- and third-order strain terms, respectively, in the elastic energy expression and the η_i are the strains.

The strain parameters have been so chosen that η_1 is proportional to the orthorhombic distortion, with $\eta_1 = 0$ corresponding to hexagonal symmetry. Therefore, when the sample is in the hexagonal phase, only the second term on the right side of Eq. (IV-2) is nonzero. The introduction of an orthorhombic distortion then leads to the appearance of two additional nonzero terms on the right side of the equation. The first of these introduces an abrupt and constant change in $d\Theta/dP$. The last term, however, involves η_1, which is a function of both temperature and pressure. It is therefore theoretically possible to obtain a variation in the pressure dependence of the Curie temperature in the orthorhombic phase. However, our experimental values of $d\Theta(B31)/dP$ appear to be constant over the range from 5 to 10 kbars, so we conclude the nonlinearity introduced by the last term is too small to be observed experimentally.

It should be emphasized, that while the above considerations have established the necessary conditions for compatibility between the observed variation in $d\Theta/dP$ and a model of strain-sensitive exchange effects giving rise to a first-order phase transition, they do not establish the sufficiency of these conditions as applied to MnAs. This will require knowledge of the elastic coefficients as well as detailed information regarding the significant magnetic exchange interactions in this material. In addition, the variation in $d\Theta/dP$ occurs abruptly over a narrow temperature interval, corresponding to a small variation in lattice parameter. This is because the large changes in Θ occur at a $B8_1$ to B31 transition where the manganese atomic moment changes from a high-spin to a low-spin value.

The sharp change in the manganese moment at T_1 indicates an equally sharp change in the intra-atomic exchange splitting Δ_{ex} of states of different spin, which is consistent with a critical Mn-Mn separation of $a_o \approx 3.7$ Å in the basal plane. For $a_o > 3.7$ Å, the symmetry is hexagonal ($B8_1$) and the band model for the d-state manifold is that shown schematically in Fig. IV-4(a).

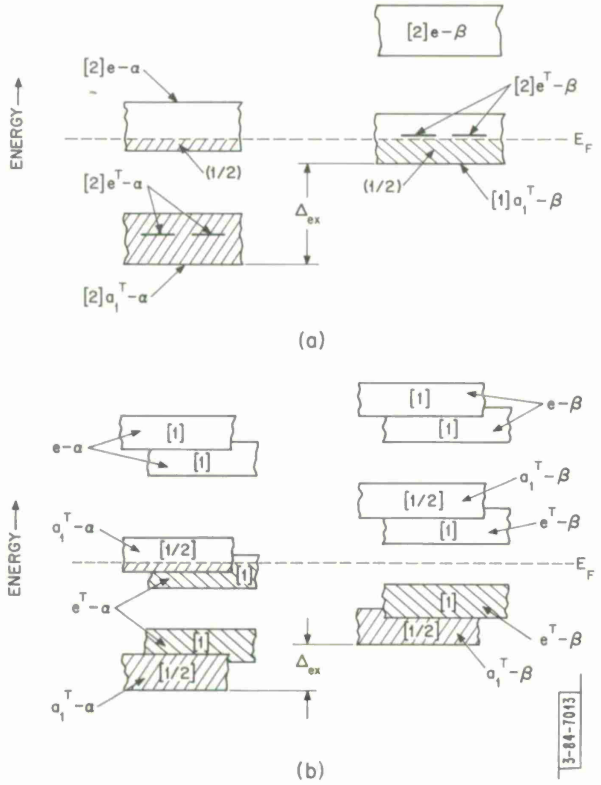

Fig. IV-4. Schematic one-electron band model for d-state manifold of MnAs. Fermi energy E_F is assumed to lie between filled and empty s, p bands which are not shown. Numbers in brackets and parentheses indicate number of orbitals and electrons, respectively, per molecule in a given band. (a) Hexagonal ($B8_1$) phase; $\mu_{Mn} = 3\mu_B$ (b) Orthorhombic (B31) phase; $1\mu_B < \mu_{Mn} < 2\mu_B$, depending on magnitude of Δ_{ex}.

The crystalline symmetry splits the atomic d-level into a collective-electron a_1^T orbital directed along the c-axis, two degenerate collective-electron e-orbitals directed toward near-neighbor anions, and two degenerate, localized-electron e^T orbitals directed toward near-neighbor cations within a basal plane. Associated with localized e^T orbitals is a large intra-atomic exchange splitting Δ_{ex} of states of different spin. Electron correlations among narrow-band electrons would produce a deep minimum in the β-spin a_1^T band, and the Fermi level is assumed to lie at this minimum. With this assumption, both the Mn-As-Mn interactions and the Mn-Mn interactions along the c-axis are ferromagnetic while the Mn-Mn interactions in the basal plane are antiferromagnetic, which is compatible with the positive exchange striction only in the basal planes at T_1. Furthermore, this gives a net spin-only ferromagnetic moment of $3.0\mu_B$, which compares favorably with the observed moment of $3.1\mu_B$.

In the orthorhombic B31 phase, $a_o < 3.7$ Å and the e^T orbitals are presumably transformed into collective-electron orbitals, thereby abruptly decreasing Δ_{ex}. Also the reduced symmetry further splits the bands, as indicated in Fig. IV-4(b). The relative occupancies of the $e^T - \alpha$ and $a_1^T - \alpha$ orbitals will determine whether there is ferromagnetic order or a complex metamagnetism, and the spin-only atomic moment for any ferromagnetic phase would be $1\mu_B$/mole.

N. Menyuk K. Dwight
J. A. Kafalas J. B. Goodenough

2. Dependence of Susceptibility Exponent upon Spin Quantum Number (Abstract Submitted to Fourteenth Conference on Magnetism and Magnetic Materials, New York)

Initially the exponent γ describing the divergence of the zero-field susceptibility, $\chi \sim (T - T_c)^{-\gamma}$ was thought to have the value 4/3 for all values of the spin quantum number S. However in 1964 it was proposed[11] that γ varies smoothly with S, roughly as $\gamma(S) = 4/3 + 0.05/S$, and as additional terms in the various high-temperature expansions became available, it was argued that[12] $\gamma(\frac{1}{2}) = 1.43 \pm 0.03$ and that[13] $\gamma(\infty) = 1.38 \pm 0.01$. An answer to the question "Is $\gamma(S) = \text{const}$ for all S?" would be extremely relevant to scaling law theories; to this end we use various extrapolation procedures not used in Refs. 12 and 13 to corroborate the values for γ quoted therein. If $\gamma(\frac{1}{2}) \neq \gamma(\infty)$, then one is led to ask further "Does $\gamma(S)$ vary <u>smoothly</u> or <u>discontinuously</u> with S as S goes from $\frac{1}{2}$ to ∞?" By incorporating the recent extension of the general-S series,[14] we present some evidence for the possibility that $\gamma(S) = 1.38$ for all $S > \frac{1}{2}$.

H. E. Stanley

3. Staggered Susceptibility of Two- and Three-Dimensional Heisenberg Antiferromagnets (Abstract Submitted to Fourteenth Conference on Magnetism and Magnetic Materials, New York)

High-temperature expansions of the <u>staggered</u> susceptibility $\tilde{\chi}$ for the Heisenberg antiferromagnet are analyzed for two- and three-dimensional lattices. For two-dimensional lattices the evidence favoring a divergent staggered susceptibility is found to be essentially as strong as that presented earlier[15] in support of a divergent susceptibility χ for the two-dimensional Heisenberg ferromagnet. Thus recent experimental[16] and theoretical[17] work on "two-dimensional antiferromagnets" appears to be supported by series expansions. For three-dimensional lattices the

susceptibility exponent $\tilde{\gamma}$ governing the divergence of the staggered susceptibility is determined and comparison is made with recent experimental measurements.

H. E. Stanley

4. Exact Solution for Linear Chain of Isotropically-Interacting Classical Spins of Arbitrary Dimensionality (Abstract Submitted to Fourteenth Conference on Magnetism and Magnetic Materials, New York)

The isotropic Hamiltonian $\mathcal{H}^{(\nu)} = -J \sum_{j=1}^{N-1} \vec{S}_j \cdot \vec{S}_{j+1}$ is considered for an open linear chain of N ν-dimensional vector spins S_j; $\mathcal{H}^{(\nu)}$ reduces to the $S = \frac{1}{2}$ Ising, planar, and Heisenberg models for $\nu = 1, 2$, and 3. The thermodynamic properties (including the susceptibility) of $\mathcal{H}^{(\nu)}$ are found for ferromagnetic ($J > 0$) and antiferromagnetic ($J < 0$) exchange interactions for all temperatures T and all spin dimensionalities ν. The manner in which the various properties depend upon T and ν is studied; in particular we find that (a) although the chain of spins does not display long-range order except at $T = 0$ for any value of ν, the various properties vary monotonically with ν [in such a way that, e.g., the degree of "short-range order" decreases with increasing ν], and (b) as the spin dimensionality increases without limit, all the calculated properties approach precisely those predicted by the Berlin-Kac spherical model.

H. E. Stanley

D. SCATTERING EXPERIMENTS WITH LASERS

1. Light Scattering from Spin Fluctuations in Magnetic Systems

Experiments are being undertaken to detect the scattering of light from long wavelength spin fluctuations in magnetic systems. Both elastic (Rayleigh) scattering near the transition temperature and inelastic (Raman) scattering over a wider temperature range are being investigated.

In the Rayleigh case, scattering arises from a modulation of the dielectric constant of the material by the spin fluctuations, through spin-orbit interaction. In ferro and ferrimagnetic systems, the scattered intensity due to these fluctuations is proportional to the magnetic susceptibility, which should diverge as

$$\frac{1}{\left(\frac{T - T_c}{T}\right)^{\gamma} + (aq)^2} \qquad \text{(IV-3)}$$

near the transition temperature T_c; here a is some exchange interaction length, and q is the scattering wave vector. Of prime interest is the measurement of γ, the exponential susceptibility coefficient. The spectrum of the scattered light reflects the time variation of the spin fluctuations, and its linewidth should vary inversely with a magnetization diffusion time, another experimental parameter to be measured.

Preliminary experiments have been performed using an argon ion laser, scattering from ferromagnetic $CrBr_3$ and ferrimagnetic $RbNiF_3$. In the former case, intense scattering from magnetic domains below the Curie temperature ($T_c = 32.5°K$) has been observed, but instability of the laser and detection system, together with large background scattering, have prevented an accurate measurement of the dynamic scattering immediately above the transition temperature.

A much smaller increase in the elastic scattering from $RbNiF_3$ has been seen below its transition ($T_c = 139°K$), but the same experimental difficulties hold.

An investigation of the Raman scattering from $RbNiF_3$ revealed, along with several optical phonon lines, an intense line shifted approximately 500 cm^{-1} from the argon laser energy. This Raman line differed from the narrow phonon lines in its width (approximately 65 cm^{-1} at $T < 50°K$ to 200 cm^{-1} at $T \simeq 140°K$) and the relatively large decrease in its shift at higher temperatures. Its persistence well above T_c tends to rule out ordinary magnon scattering as the source, but the position and width suggest that it may arise from localized spin-flip transitions involving strongly coupled spin pairs which tend to remain aligned even above T_c. Attempts are being made to compute the spin wave dispersion relations, and determine exchange constants consistent with experimental data.

S. R. Chinn
H. J. Zeiger

2. High Resolution Raman Scattering in Quartz

The 128-cm^{-1} Raman vibration in quartz is a doubly degenerate E-mode infrared active in the ordinary ray. The coupling to the infrared removes the degeneracy, splitting the mode into longitudinal and transverse parts with a gap given by

$$\Delta\omega = \omega_L - \omega_T = \omega_T\left(\sqrt{\epsilon_o/\epsilon_\infty} - 1\right) \simeq \omega_T \frac{S}{2\epsilon_\infty} \quad . \tag{IV-4}$$

Here ϵ_o and ϵ_∞ are the dielectric constants below and above the resonance and S is the oscillator strength.

S has been measured at room temperature[18] for this mode; the corresponding gap is 0.1 cm^{-1} This is much smaller than the 300°K linewidth, $\delta\omega$, of ~4 cm^{-1} so the doublet cannot be resolved. This 128-cm^{-1} vibration is the lowest lying optical mode; so at low temperatures its linewidth is expected to decrease markedly since the vibration can only decay into a rather low density of acoustic phonon states. However, it is known that the infrared oscillator strength also decreases at low temperatures,[19] and it is the purpose of this report to relate measurements of the linewidth and gap at liquid helium temperatures by high resolution Raman scattering.

The experimental arrangement is similar to that used by Clements and Stoicheff,[20] where the backscattered Raman-shifted light is isolated by interference filters and the spectral shape is analyzed with a pressure-scanned Fabry-Perot interferometer. Typical traces for phonons propagating along three crystal axes are shown in Fig. IV-5.

The scattering axis and the incident and scattered light polarizations have been confined to the plane perpendicular to the c-axis of quartz. Examination of the Raman tensor and phonon polarization given by Loudon[21] demonstrates that the scattered intensity from the longitudinal branch goes as $C_L \cos^2 3\psi$ and the transverse branch as $C_T \sin^2 3\psi$, where ψ is measured between the x-crystal axis and the phonon wave vector. C_L need not be equal to C_T since there is an interference between the deformation potential and electro-optic contributions to the LO scattering, whereas only the former contributes to the TO branch.

Analysis of the data in Fig. IV-5 yields the following results for 5°K. $(C_L/C_T) = 0.8 \pm 0.3$, $\delta\omega = 0.05 \pm 0.01$ cm^{-1}. $\Delta\omega = 0.02 \pm 0.01$ cm^{-1}. Thus the doublet is still unresolvable; the value of the gap can be determined only by the broadening of the [110] spectrum.

A. S. Pine

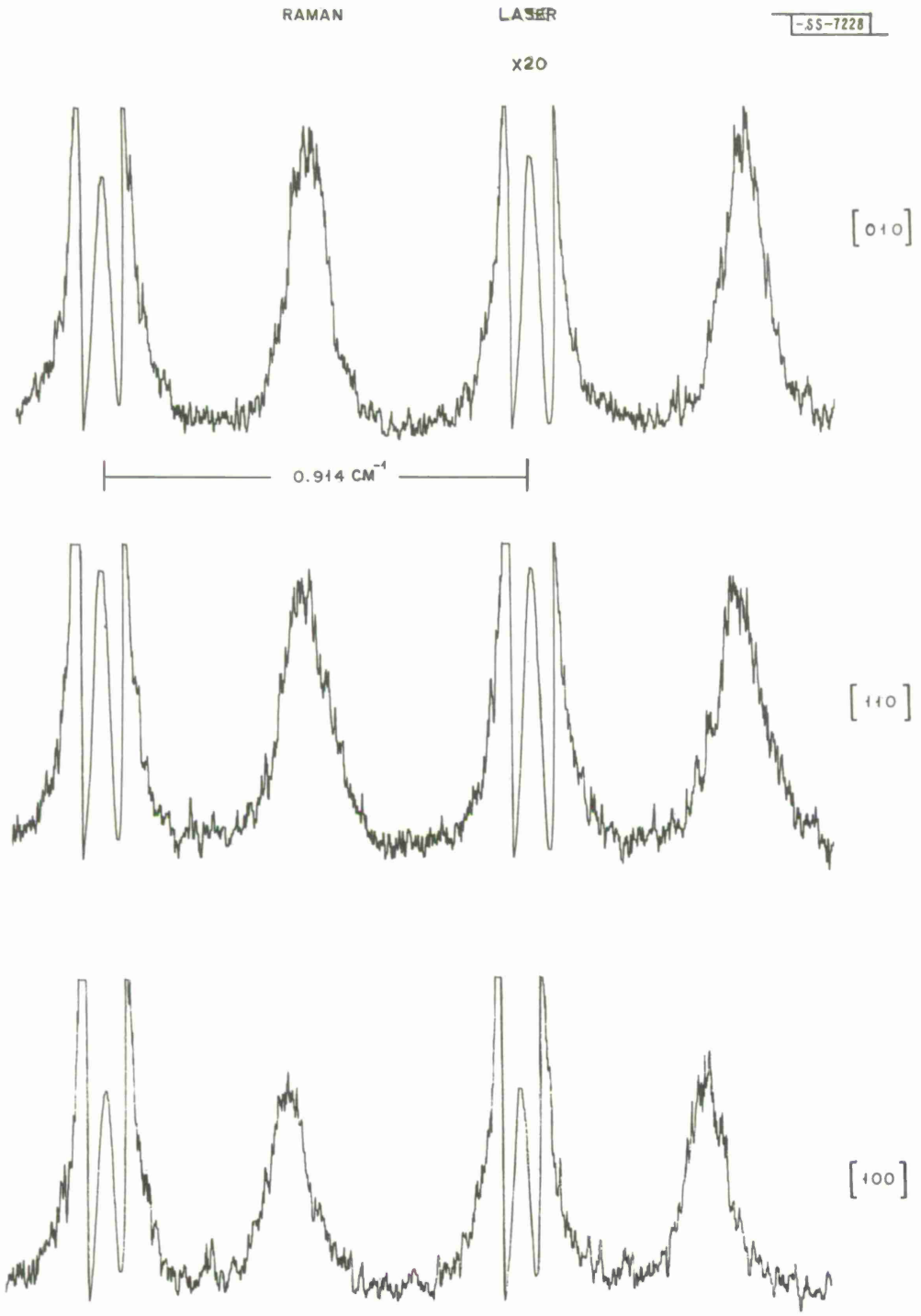

Fig. IV-5. High resolution, low temperature Raman scattering in quartz; 128 cm^{-1} mode, 5°K, backscattering along axis marked; polarizations ordinary.

REFERENCES

1. Solid State Research Report, Lincoln Laboratory, M.I.T. (1967:2), p. 32, DDC 656548, H-853.
2. A.L. Jain, Phys. Rev. 144, 1518 (1959).
3. M.R. Ellett, R.B. Horst, L.R. Williams and K.F. Cuff, (Proc. Intern. Conf. Phys. Semicond., Kyoto, 1966) J. Phys. Soc. Japan, 21, Supplement 666 (1966).
4. P. Resibois, Phys. Rev. 138, B281 (1965); Bull. Acad. Roy. Belg. 50, 1287 (1964).
5. J.M. Luttinger and W. Kohn, Phys. Rev. 109, 1892 (1958).
6. R.H. Wilson and J.S. Kasper, Acta Cryst. 17, 95 (1964).
7. C. Guillaud, J. Phys. Rad. 12, 223 (1951).
8. Solid State Research Report, Lincoln Laboratory, M.I.T. (1968:2), p. 49, DDC 672961, H-888.
9. C.P. Bean and D.S. Rodbell, Phys. Rev. 126, 104 (1962).
10. D.S. Rodbell and C.P. Bean, J. Appl. Phys. Suppl. 33, 1037 (1962).
11. H.E. Stanley and T.A. Kaplan, unpublished; J. Appl. Phys. 38, 977 (1967).
12. G.A. Baker, H.E. Gilbert, J. Eve and G.S. Rushbrooke, Phys. Rev. 164, 700 (1967).
13. H.E. Stanley, Phys. Rev. 158, 546 (1967).
14. R.L. Stephenson, K. Pirnie, P.J. Wood and J. Eve, Phys. Letters 27A, 2 (1968).
15. H.E. Stanley and T.A. Kaplan, Phys. Rev. Letters 17, 913 (1966).
16. G. de Vries, D.J. Breed, E.P. Maarschall, and A.R. Miedema, J. Appl. Phys. 39, 1207 (1968); A.R. Miedema, et al. (to be published).
17. M.E. Lines, Phys. Rev. 164, 736 (1967).
18. E.E. Russell and E.E. Bell, J. Opt. Soc. Am. 57, 341 (1967).
19. J.N. Plendl, et al., J. Phys. Chem. Solids 28, 1589 (1967).
20. W.R.L. Clements and B.P. Stoicheff, Appl. Phys. Letters 12, 246 (1968).
21. R. Loudon, Advan. Phys. 13, 423 (1964).

DOCUMENT CONTROL DATA – R&D

(Security classification of title, body of abstract and indexing annotation must be entered when the overall report is classified)

1. ORIGINATING ACTIVITY *(Corporate author)* Lincoln Laboratory, M.I.T.	2a. REPORT SECURITY CLASSIFICATION Unclassified 2b. GROUP None

3. REPORT TITLE

Solid State Research

4. DESCRIPTIVE NOTES *(Type of report and inclusive dates)*

Quarterly Technical Summary – 1 May through 31 July 1968

5. AUTHOR(S) *(Last name, first name, initial)*

McWhorter, Alan L.

6. REPORT DATE	7a. TOTAL NO. OF PAGES	7b. NO. OF REFS
15 August 1968	64	67

8a. CONTRACT OR GRANT NO. AF 19(628)-5167 b. PROJECT NO. 649L c. d.	9a. ORIGINATOR'S REPORT NUMBER(S) Solid State Research (1968:3) 9b. OTHER REPORT NO(S) *(Any other numbers that may be assigned this report)* ESD-TR-68-246

10. AVAILABILITY/LIMITATION NOTICES

This document has been approved for public release and sale; its distribution is unlimited.

11. SUPPLEMENTARY NOTES	12. SPONSORING MILITARY ACTIVITY
None	Air Force Systems Command, USAF

13. ABSTRACT

This report covers in detail the solid state research work at Lincoln Laboratory for the period 1 May through 31 July 1968. The topics covered are Solid State Device Research, Optical Techniques and Devices, Materials Research, and Physics of Solids.

14. KEY WORDS

solid state devices
optical techniques and devices
materials research
electron band structure
magnetism
laser research
infrared
photovoltaic detectors
crystal growth
magnetoreflection
magneto-optical research
magnetoabsorption
laser scattering
Raman scattering

Printed by
United States Air Force
L. G. Hanscom Field
Bedford, Massachusetts